A Mixed Eulerian-Lagrangian scheme for scalar transport

Benoît Trouette, Georges Halim Atallah, Stéphane Vincent

A Mixed Eulerian-Lagrangian scheme for scalar transport

Benoît Trouette✉, Georges Halim Atallah, Stéphane Vincent

Univ Gustave Eiffel, CNRS, MSME UMR 8208,
F-77454 Marne-la-Vallée, France

Version: June 17, 2020

Contents

✉ corresponding author: trouette@u-pem.fr

Abstract

The tracking of pollutants in gas and liquid is a major problem to address in atmospheric environment, air quality characterization and industrial material processes. A Lagrangian scheme devoted to the approximation of the advection term in an advection-diffusion equation is proposed to deal with small diffusivity values or large Péclet numbers. The Lagrangian scheme is used in practice as an Eulerian method discretized on Lagrangian marker points. Advection and diffusion of a circular concentration spot in a vortex flow are considered for validation purpose. The resulting mixed Eulerian-Lagrangian scheme reduces the numerical diffusion to almost computer error and provides better results than other Eulerian classical schemes of the literature. The scheme is finally illustrated in a natural convection situation.

Keywords: Advection-diffusion; Finite volume; Incompressible flow; Natural convection; Mixed Eulerian-Lagrangian scheme; Scalar transport

1 Introduction

The modeling and simulation of pollutant or chemical species transport in gaseous or liquid surrounding media are of primary importance for various applications such as indoor air quality [27], occupational health [14, 16], urban air pollution [31], transport of tracers through permeable sediments [23] or Carbone Fiber Composite (CFC) material design [10]. When a low diffusivity is considered or for high velocity flow regimes, the resulting Péclet number is high, testifying that advection is predominant in the concentration transport equation against diffusion. Among high Péclet number flows, we can quote forced convection in differentially heated channels [8], the transport of pollutants in aquifers [38], liquid-liquid extraction in chemical engineering processes [13] or mixing of pure and polluted liquids for material design applications [2, 7]. As soon as an Eulerian model is chosen for the concentration evolution over time, i.e., an advection-diffusion equation (ADE), which is the case in most applications, the discretization of the scalar ADE requires developing specific schemes as soon as the Péclet number is high. Indeed, in these configurations, the hyperbolic nature of the equation dominates the scalar problem.

The design of schemes for the hyperbolic advection term of the transport equation for pollutant concentration has been widely studied, with mostly Eulerian schemes relying on spline reconstruction, high-order spectral, finite difference and finite volume schemes, combined with limiters belonging to the class of TVD or WENO approaches. Reviews and comparisons of these schemes are, for example, given in [18, 31, 42]. Outside the framework of atmospheric applications, a lot of works have been also conducted in the community of applied Mathematics, which are reported and synthesized, for example, in [19]. Combination of TVD and WENO schemes together with Runge Kutta schemes, proposed for dealing with hyperbolic equations, is also available (see for example [44]) for reducing the CPU cost compared to pure WENO schemes while maintaining a good accuracy. Other sophisticated schemes can be applied to the advection term of a transport equation, with slightly better results than standard WENO schemes.

Among them, we can cite the semi-Lagrangian multi-moment finite volume method with fourth-order WENO projection [40], the Lagrangian modeling of advection-diffusion transport in open channel flow by [9] that is very accurate at high Péclet number but only presented in 1D applications and also the Adaptive Mesh Refinement (AMR) TVD scheme [7]. The conclusion of all studies is that when the molecular or turbulent diffusion is low compared to advection, all schemes are diffusive or dispersive, providing unexpected spreading or nonphysical oscillations of the numerical solutions. In the present work, a hybrid Lagrangian scheme [42], previously applied to advection, is improved for the ADE that avoids numerical diffusion and respects to some extent, but not in the mathematical sense, the monotonicity of the solution. The initial idea for the design of our scheme was inspired by several pioneer works:

- The Particle-in-Cell-method (PIC) initially developed by the team of F.H. Harlow at Los Alamos [17] is based on the spatial domain mapped by an Eulerian mesh, as it is classically achieved with finite volumes, finite differences or finite elements. Each Eulerian cell brings physical variables such as pressure or fluid velocity. Lagrangian marker particles are seeded in the Eulerian cells. They represent fluid elements that move through the Eulerian mesh and interact with other fluid elements in a procedure that couples the two materials together. Reseeding or remeshing procedures are used to maintain a certain number of particles in cells and thus a good precision [4], and also transfer techniques between Eulerian and Lagrangian representations, built based on interpolation, shape or kernel functions. Intermediate or fictitious time variables are finally introduced to be able to solve Lagrangian part of the transfers (mainly number density, current density, advection or convection) and also Eulerian ones (diffusion for example). These approaches have been extensively used for plasma physics and electromagnetism but also for compressible flows and solid mechanics.

- The Smooth Particle Hydrodynamics (SPH) approach [20, 30] is a computational method to simulate fluid flows. It has been used in many areas of research, including astrophysics, ballistics, volcanology and oceanology to cite but a few. It belongs to the family of full Lagrangian methods. It consists in advecting a set of particles as a kind of Lagrangian mesh. Thanks to these Lagrangian control points, a mapping is built with quadrature formulae, weighted approximations and kernel functions. These reconstructed variables are then derived or used to solve the conservation equations. In SPH, particles are bestowed with volume, mass, momentum, temperature, concentration or any other hydrodynamic property. Various examples and applications are illustrated, for example, in [36] concerning air/water flows interacting with an airplane, sloshing in a compartment tank of a fluid cargo, aquaplaning of a car tire or filling patterns predicted for high pressure die casting.

- Other more specific and interesting Lagrangian techniques are the Particle Strength Exchange (PSE) and the Lagrangian Filtered Density Function (FDF) approaches.
  The PSE has been used to solve two-dimensional pollutant transport in porous media [45]. The main idea is to introduce regularization functions to approximate integral analytical solutions of the diffusion or dispersion operators.
  On the other hand, combined with Large Eddy Simulation (LES) models of turbulence,

the FDF method has been also applied to pollutant transport [43]. The FDF/LES is used to account for the near-wall molecular transport. It is evaluated on a heated channel flow and compared with DNS data.

A review of various existing Lagrangian schemes available in the literature was written by Koumoutsakos [24].

The main purpose of the present work is to present a Lagrangian scheme for advection and its coupling to an Eulerian solving of diffusion. Several important steps are required for designing the Lagrangian scheme, such as marker seeding and reseeding over time, Lagrangian transport of the markers, velocity interpolation from the Eulerian Navier-Stokes grid to the marker positions, projection of the Lagrangian concentration field to the Eulerian grid and treatment of boundary conditions. The novelty of the resulting Mixed Eulerian-Lagrangian (MEL) method introduced in this paper, in particular compared to PIC methods, is that the particles seeded in cells are used to approximate the advective part of advection-diffusion equation in some kind of Lagrangian Method Of Characteristic (MOC) scheme [35], whereas in classical PIC approaches, the particles are used to solve different physics (plasma, electromagnetism, ...) than the Eulerian mesh. In the proposed approach, the physical information provided by the Lagrangian markers feeds the Eulerian located variables and reciprocally. In addition to these discretization aspects, validation problems have been chosen, some with analytical solutions, in order to demonstrate the capacity of the new mixed Lagrangian-Eulerian scheme for ADE solving to provide better results as soon as the Péclet number is high or the mesh resolution is low, or both. A conceptually similar approach to our scheme, combining Lagrangian treatment of the advection and Eulerian discretization of diffusion, is reported in the work of [39]. It is based on a semi-Lagrangian Crank-Nicolson scheme. Applied to analytical scalar advection test cases, it provides monotonic solutions but induces numerical diffusion, that is not present in our scheme when diffusion is negligible.

The structure of this manuscript is as follows. In Sect. 2, the model and numerical methods considered for handling the simulation of concentration transport are briefly presented, laying emphasis on a new Lagrangian scheme proposed for tackling the advection part of the ADE. In particular, the coupling between the Lagrangian treatment of advection and Eulerian solving of diffusion is discussed as well as reseeding operations for Lagrangian scheme markers. Thereafter, Sect. 3 is devoted to validating the new Lagrangian-Eulerian scheme for ADE on various problems such as 2D advection-diffusion of a concentration peak, concentration spot in 2D and 3D sheared velocity fields and 2D natural convection at moderate Rayleigh number. Conclusions and perspectives are finally drawn in Sect. 4.

2 Model and numerical methods

2.1 Generalities

The present approach is developed within the framework of incompressible fluid flows simulated with the Finite-Volume method on Cartesian staggered grid [17]. It can be extended straight-

forwardly to collocated grids without loss of generality. Concerning scalar evolution over time, the following Eulerian ADE is considered

$$\frac{\partial \Phi}{\partial t} + \vec{\nabla} \cdot (\vec{u}\Phi) = \vec{\nabla} \cdot (\Gamma \vec{\nabla} \Phi) \tag{1}$$

where Φ is the advected field (temperature, concentration, ...), Γ its diffusivity and $\vec{u}$ the fluid velocity, either prescribed or given by the last iteration of the Navier-Stokes resolution. Classical Eulerian centered, upwind, QUICK, TVD or WENO schemes are generally used to discretize the advection term. It is worth mentioning that solving Eq. (1) with centered scheme introduces oscillations and unbounded solutions for low diffusivity coefficient Γ or high values of the Péclet cell number given by $Pe_c = \|\vec{u}\|\Delta x/\Gamma$. On the contrary, low order upwind like schemes are Total Variation Diminishing (TVD). However, they generate an important numerical diffusion that alters the physical meaning of the solution, as centered scheme does.

In the method proposed here, contrary to classical schemes that consider the whole Eq. (1) with explicit, implicit or mixed discretizations, we have chosen to split the equation into two unsteady equations: on the one part the advection and the diffusion on the other part. Indeed, the new approach for approximating ADE does not directly solve Eq. (1), it uses a sequential operator splitting method [3, 12]. Introducing a time step Δt, the solution of Eq. (1) is marched in time according to two sub-steps. First, the advection equation

$$\frac{\partial \Phi}{\partial t} + \vec{\nabla} \cdot (\vec{u}\Phi) = 0 \tag{2}$$

is solved on the time interval $]t, t + \Delta t]$ and provides the intermediate solution $\Phi^\star$. Then, the unsteady diffusion equation

$$\frac{\partial \Phi}{\partial t} - \vec{\nabla} \cdot \left(\Gamma \vec{\nabla} \Phi\right) = 0 \tag{3}$$

is treated on the same time interval $]t, t + \Delta t]$ with the initial condition $\Phi(t) = \Phi^\star(t + \Delta t)$ and provides the approximated solution of $\Phi(t+\Delta t)$. The sequential operator splitting method used here is second-order accurate at each time step and first-order accurate when it is applied to update the solution from $t = 0$ to the final time t_{end} [3]. Note that more sophisticated operator splitting methods and their properties can be found in [3, 12].

The time discretization introduces the following notations: For the sake of simplicity (not restrictive), a constant time step, compatible with the CFL condition, is here considered. $\Phi^n = \Phi(t^n)$ is the discrete value of Φ at time $t^n = t^0 + n\Delta t$, n is the iteration number, and $\Delta t = t^{n+1} - t^n$ is the time step. In practice, the post-advection intermediate solution $\Phi^\star$ is updated solving Eq. (2) with an explicit scheme (see below), while Eq. (3) is discretized with an implicit centered spatial scheme. The resulting linear system is resolved by using direct solvers (MUMPS [1]) or iterative Bi-CGSTAB II solvers [46] preconditioned under Jacobi or MILU techniques [15]. In addition to the mixed Eulerian Lagrangian scheme developed in this paper, the Lax-Wendroff TVD scheme with a Superbee limiter [41] and conservative or non-conservative WENO schemes of order 5 [5, 21, 37] will be used to solve Eq. (2), both coupled with a third order Runge-Kutta TVD time integration. For comparison purposes, classical implicit centered and upwind schemes, that directly resolve Eq. (1), are also presented.

2.2 Scales analysis

Advection diffusion problems involve two characteristic length scales. The advection scale corresponds to a distance $L = V_0 t$, where V_0 is the fluid velocity, while the diffusion scale δ is linked to the boundary layer growth rate. As δ varies as $K\sqrt{\Gamma t}$, where the constant K depends on the studied problem, the dimensionless parameter characterizing the problem is the ratio

$$\eta = \frac{L}{K\sqrt{\Gamma t}} \tag{4}$$

For K of the order of unity, a diffusivity of 10^{-6} m^2/s and $t = 1$ s, the diffusive length scale is about $\delta \approx 10^{-3}$ m. In problems where the advective length scale is about 1 meter, the ratio η between advection and diffusion is at least three orders of magnitude. Note that, the K value is chosen here as the unity to simplify the scale analysis, but the correct value according to the considered problem will be specified in the next sections.

2.3 Mixed Eulerian-Lagrangian scheme for advection-diffusion

A Mixed Eulerian (for diffusion) - Lagrangian (for advection) (MEL) scheme is proposed as an extension of the Volume of fluid Sub-Mesh (VSM) scheme from [42]. The main interest of this approach is to avoid numerical diffusion in the advection step when advection is predominant. For the sake of simplicity, the scheme is here presented on a regular grid. Few adjustments have to be considered to deal with irregular Cartesian grids and unstructured meshes.

2.3.1 General treatment

A number of M markers (Lagrangian particles) of positions $\vec{X}_m$, $m = 1, \ldots, M$, and volumes δV_m, are seeded in the Eulerian grid (Fig. 1) devoted to solving the conservation equations. The volumes δV_m used here have no physical meaning, but they allow, as it will be shown later, to use weighted averages for the reconstruction of the Eulerian values Φ. Initially, the markers are equally placed in each cell according to a number of particles per direction and per cell, or particle density number, P; a simulation then handles $M = P^d \times N_x \times N_y \times N_z$ Lagrangian objects, where d is the space dimension and N_x, N_y and N_z are the numbers of Eulerian mesh cells in each space direction. Note that in 2D applications $N_z = 1$. Furthermore, the markers carry a local information, noted ϕ_m, associated with the Eulerian field Φ. At the initial time,

$$\phi_m^0 = \Phi^0(\vec{X}_m^0) \tag{5}$$

With the knowledge of the velocity $\vec{u}|_{\vec{X}_m}$ at the position of the particle, the markers are then advected solving the Lagrangian equation:

$$\frac{d\vec{X}_m}{dt} = \vec{u}|_{\vec{X}_m} \tag{6}$$

For a second-order Runge-Kutta Euler scheme, the time integration starts with a prediction of the solution using a first order Euler scheme:

$$\vec{X}_m^\star = \vec{X}_m^n + \Delta t \; \vec{u}^n|_{\vec{X}_m^n} \tag{7}$$

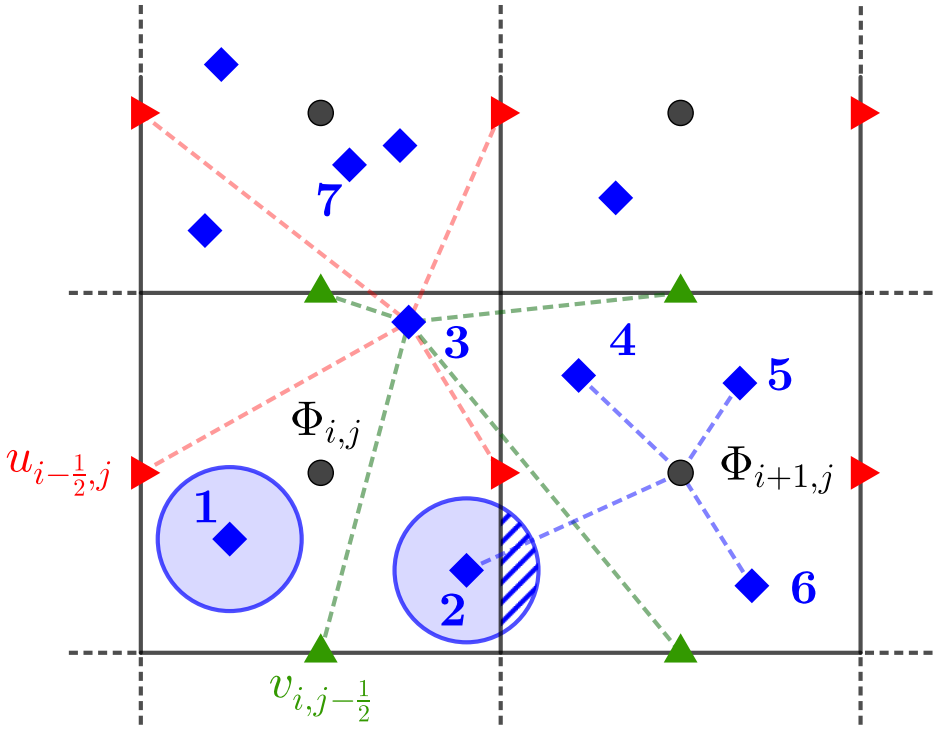

Figure 1: Sketch of the Lagrangian particles (blue diamond) on the 2D staggered regular grid used to discretize the incompressible Navier-Stokes equations. Velocities at particle position are interpolated with surrounding grid velocities (see marker 3 for example, red right triangles and green triangles stand for horizontal and vertical components, respectively). Filled blue region denotes the volume δV carried by a particle (shown for particles 1 and 2). The dashed blue surface stands for the part of the volume assigned to the neighboring cell. The Eulerian information is computed with averages of markers included in the corresponding cell (see cell $\Omega_{i+1,j}$ surrounding $\Phi_{i+1,j}$ for example).

where $\vec{u}^n|_{\vec{X}_m^n}$ is the fluid velocity interpolated from the surrounding velocity points at the particle position (see Fig 1). The second step reads formally:

$$\vec{X}_m^{n+1} = \frac{1}{2}\left(\vec{X}_m^n + \vec{X}_m^\star\right) + \frac{1}{2}\Delta t\ \vec{u}^{n+1}|_{\vec{X}_m^{n+1}} \tag{8}$$

In the framework of the Navier-Stokes resolution, the velocity $\vec{u}^{n+1}$ is generally unknown at this step. Except for the first time step where $\vec{u}^{n+1} = \vec{u}^n$ is forced, a classical linear extrapolation in time is used: $\vec{u}^{n+1}$ is approximated by $2\vec{u}^n - \vec{u}^{n-1}$. Furthermore, in the right-hand side of Eq. 8, the position $\vec{X}_m^{n+1}$ to which the velocity has to be interpolated is also unknown. It is approximated by the intermediate position value $\vec{X}_m^\star$. Finally, Eq. (8) can be written as

$$\vec{X}_m^{n+1} = \frac{1}{2}\left(\vec{X}_m^n + \vec{X}_m^\star\right) + \frac{1}{2}\Delta t\ (2\vec{u}^n - \vec{u}^{n-1})|_{\vec{X}_m^\star} \tag{9}$$

The interpolations at particle positions (initial and intermediate) are then carried out either with the Parabolic Edge Reconstruction Method (PERM) [29] (needs a five point stencil per direction) or with a classical linear $Q1$ method near domain boundaries.

The two-step second-order Runge-Kutta (RK) scheme (Eqs. (7) and (8)) used here is formally third-order accurate at each time step and second order accurate over multiple time steps.

With a given velocity field, it has been checked numerically that the second-order accuracy is obtained for the particle positions and velocities. Using high-order RK methods improves the accuracy of these quantities but does not improve significantly the global solution (additional numerical tests have been achieved with RK2 mid-point, RK3, RK4 and Velocity-Verlet schemes). An explanation is that the Eulerian field is built from averages of the marker local values ϕ_m which are not directly dependent on the particle positions and velocities. Indeed, ϕ_m is unaffected over the Lagrangian time integration regardless of the choice of the time integrator; the use of high-order and/or more sophisticated schemes is then not justified/useful. The RK2 Euler scheme is in our case the best compromise between accuracy and number of operations involved.

The post-advection value of the Eulerian field Φ is evaluated with weighted averages on each cell $\Omega_{i,j,k}$. Formally, it reads:

$$\Phi^{\star}_{i,j,k} = \frac{\sum_{m=1}^{N_p} \phi^n_m \delta V'_m}{\sum_{m=1}^{N_p} \delta V'_m} \qquad \text{with} \quad \delta V'_m = \delta V_m \cap \Omega_{i,j,k} \tag{10}$$

where N_p and $\delta V'_m$ are the particle number and the overlapping associated volume belonging to the cell, respectively. As illustrated in Fig. 1 with particle 2, due to its associated volume δV_m, a marker can contribute to the computation of $\Phi^\star$ on neighboring cells. Practically, as it is difficult to handle overlapping volume in 3D grids for spherical particles and spherical shapes do not bring a complete conformal mapping of the physical space, the volumes are assumed to be boxes, defined by $\delta V = \Delta x \Delta y \Delta z^{d-2}/P^d$. The initial volume of particles contained in a cell is then equal to the cell volume. If markers were only considered as point particles, i.e., their volumes $\delta V \to 0$, Eq. (10) would simply resume as an arithmetic mean. Note that this simple treatment allows the MEL scheme to be easily applied to irregular meshes. The main additional difficulty is to use an efficient searching procedure in order to get the cell index associated with the particle position on the irregular mesh.

The value of Φ^{n+1} is then obtained solving the unsteady diffusion Eq. (3) formulated as follows in semi-discrete form, i.e., $\frac{\Phi^{n+1}-\Phi^\star}{\Delta t} - \vec{\nabla} \cdot \left(\Gamma \vec{\nabla} \Phi^{n+1} \right) = 0$. After this Eulerian diffusion step, the advection-diffusion equation (1) has been approximated on the Eulerian mesh at time t^{n+1}. This means that Φ^{n+1} is known. On a Lagrangian point of view, only the advection of the markers has been solved. That is to say that the Lagrangian value brought by the markers is only advanced in time with respect to advection, i.e., only $\phi^\star_m = \phi^n_m$ is known at the new marker positions $\vec{X}^{n+1}_m$. So, to finally obtain ϕ^{n+1}_m at the Lagrangian level of representation, the diffusion has to be added to the value brought by the markers. This is achieved by adding to ϕ^n_m, the value advected by the marker at position $\vec{X}^{n+1}_m$, the difference between the Eulerian values Φ^{n+1} and $\Phi^\star$, respectively, after and before the diffusion step:

$$\phi^{n+1}_m = \phi^n_m + \Phi^{n+1}(\vec{X}^{n+1}_m) - \Phi^\star(\vec{X}^{n+1}_m) \tag{11}$$

With this updating of the Lagrangian value, it is assumed that the diffusion is homogeneous in a given Eulerian cell at the Lagrangian scale.

Note that except in special cases, the number of particles per cell, M_c, varies over time. On the one hand, this number can increase over a value that corresponds to a total marker volume larger than the physical volume of a given cell. This number of particles per cell has to be discussed. It can be interesting to remove particles in order to save computational time. On the other hand, the information of the Eulerian cell cannot be built if there is no particle. Due to these considerations, M_c is reduced to a constant value at each iteration. For that purpose, the following reseeding treatments are applied at the beginning of the time step:

(R_1) In each cell where $M_c > P^d$, the distances between particles and their neighbors are computed for every pair. The marker having the lower norm, defined by

$$dist_m = \sum_{i \neq m}^{M_c} \|\vec{X}_m - \vec{X}_i\|^2 \tag{12}$$

is removed (particle 7 in Fig. 1), and this procedure is applied until $M_c = P^d$.

(R_2) In cells where $M_c < P^d$, new particles are randomly introduced until $M_c = P^d$.

The main interest of the reseeding procedures is to ensure that the advection is always described by several markers and also that a controlled number of markers are present in a given cell. As numerically shown in the following section, these reseeding operations can lead to spurious effects. Referring to the sketch shown in Fig. 2, a simplified description of the behavior of the reseeding treatments is presented here. At the beginning of the time step, the Eulerian value Φ^n came from an averaging on the markers in the cell and the diffusion process during the previous time step.

- When the insertion of a marker occurs (treatment (R_1)), here marker 4, its value is chosen as $\phi_4 = \Phi_i^n$. The difference to the "solution" (blue line) is denoted $\Delta\phi$. In the case of a flow oriented to the right ($u > 0$), the marker will be advected in the cell Ω_{i+1} and will generate, in this example, an over-estimated averaged value $\Phi_{i+1}^\star$ after the advection process.

- In the case of a removal (treatment (R_2)), for example marker 7 in the cell Ω_{i+1}, the consequence is the same; the post averaged advected value $\Phi^\star$ can present over- or underestimated values.

Note that these spurious effects are important when i) markers are introduced far away from those already present in the cell, ii) only few markers map the cell and iii) high gradients are present. In any cases, a solution to reduce spurious effects linked to the reseeding methods is to choose a sufficiently large number of markers per cell. This point is discussed in Sect. 3.

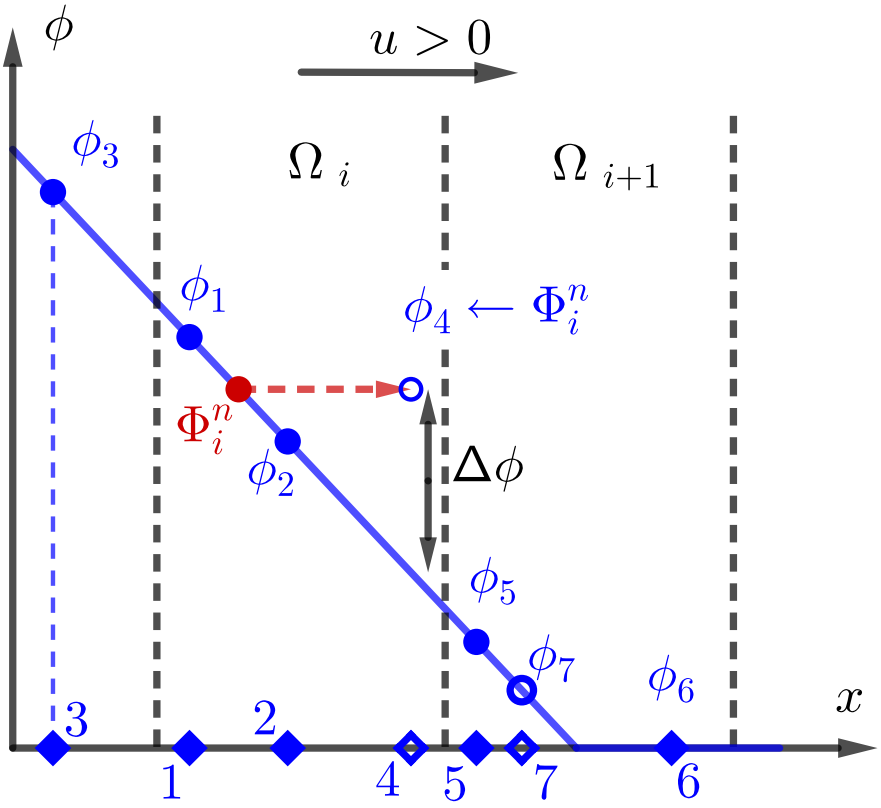

Figure 2: 1D sketch of the spurious effects linked to the reseeding methods. Markers unaffected by the insertion and removal processes are denoted with a blue filled diamond, while empty symbols (4 and 7) stand for treated markers. The insertion (R_1) treatment is illustrated with marker 4 in cell Ω_i, while removal (R_2) treatment involves marker 7. The thick blue line denotes a reference solution. The Eulerian value carried by the markers in cell Ω_i is $\Phi_i^n = 1/2(\phi_1 + \phi_2)$. This Eulerian value is affected by new created marker value like ϕ_4, in order to respect the mean value of the cell, i.e., $\Phi_i^n = \frac{1}{2}(\phi_1 + \phi_2) = \frac{1}{3}(\phi_1 + \phi_2 + \phi_4)$.

2.3.2 Algorithm

In order to clarify the method and the operator splitting, the schematic Algorithm 1 resumes the above presentation of the Mixed Eulerian-Lagrangian scheme for advection-diffusion equation.

Algorithm 1 Pseudo code for the Mixed Eulerian-Lagrangian scheme for ADE

1: $\vec{u}^{n+1} \leftarrow \vec{u}^0$
2: $\Phi^{n+1} \leftarrow \Phi^0$
3: $\phi_m^0 = \Phi^0(\vec{X}_m^0)$ ▷ Eq. (5)
4: **procedure** TIME EVOLUTION
5: **for** $n = 1$ to $t_{end}/\Delta t$ **do** ▷ $n \in \mathbb{N}^+$
6: $t^{n+1} \leftarrow t^n + \Delta t$
7: $\vec{X}^n \leftarrow \vec{X}^{n+1}$
8: $\vec{u}^n \leftarrow \vec{u}^{n+1}$
9: $\Phi^n \leftarrow \Phi^{n+1}$
10: $\phi^n \leftarrow \phi^{n+1}$
11: **procedure** LAGRANGIAN SCALAR ADVECTION
12: **inputs:** $\vec{X}_m^n$, $\vec{u}^n$, ϕ_m^n
13: **outputs:** $\vec{X}_m^{n+1}$, $\Phi^\star$
14: APPLY RESEEDING PROCEDURES ▷ (R_1) and (R_2)
15: **for** $m = 1$ to M **do** ▷ $m \in \mathbb{N}^+$
16: $\vec{X}_m^{n+1} \leftarrow$ UPDATE MARKER POSITIONS$(\vec{X}_m^n, \vec{u}^n)$ ▷ Eqs. (7) and (9)
17: $\Phi^\star \leftarrow$ COMPUTE AVERAGES$(\vec{X}_m^{n+1}, \phi_m^n)$ ▷ Eq. (10)
18: **end for**
19: **end procedure**
20: $\Phi^{n+1} \leftarrow$ EULERIAN SCALAR DIFFUSION$(\Phi^\star)$ ▷ Eq. (3)
21: **procedure** UPDATE MARKERS
22: **inputs:** $\vec{X}_m^{n+1}$, Φ^{n+1}, $\Phi^\star$, ϕ_m^n
23: **outputs:** ϕ_m^{n+1}
24: **for** $m = 1$ to M **do** ▷ $m \in \mathbb{N}^+$
25: $\phi_m^{n+1} \leftarrow$ UPDATE $\phi(\vec{X}_m^{n+1}, \Phi^{n+1}, \Phi^\star, \phi_m^n)$ ▷ Eq. (11)
26: **end for**
27: **end procedure**
28: $\vec{u}^{n+1} \leftarrow$ UPDATE VELOCITY FIELD$(\vec{u}^n, \Phi^{n+1})$ ▷ Navier-Stokes resolution
29: **end for**
30: **end procedure**

In the case where an Eulerian explicit scheme is used, the scalar advection procedure (line 11 in Algorithm 1) is substituted by the explicit resolution of Eq. (2) and the update marker procedure (line 21) is not performed. In order to optimize the computation time, linked list and cell list storage techniques, widely used in molecular dynamics simulations (see for example Chap. 3. of [33]), are adapted to manage the Lagrangian markers in the Eulerian cell neighborhood.

2.3.3 Boundary conditions

As suggested above, boundary conditions are needed during the unsteady diffusion equation (3) resolution. The operator splitting and the Lagrangian method proposed to deal with the advection part (Eq. (2)) introduce a need to tackle the Eulerian boundary conditions with respect to the Lagrangian markers. Both the values they carry or their velocities and positions can be affected. To clarify the adopted treatment, Fig. 3 is proposed for the sake of clarity and

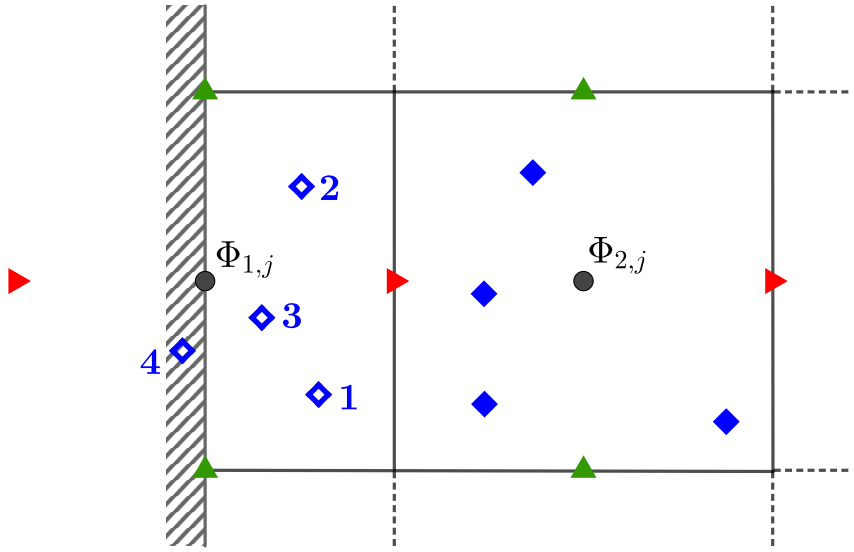

Figure 3: Zoom near a physical boundary. The update (Eq. (11)) of particle local information ϕ in boundary cells (blue empty diamonds) is modified. Markers outside the domain boundaries are turned off during the time integration process.

a boundary cell $(i = 1, j)$ is considered. Note that the staggered grids used in our approach have the specificity that the scalar nodes are on the physical boundaries (see Fig. 3).

Management of markers

As markers are fluid flow tracers, they follow trajectories. If the incompressibility constraint were fully satisfied at a discrete level, the markers would not cross wall boundaries. Due to interpolation errors of marker velocities that do not satisfy divergence-free properties in a conservative sense but just on a local sense for PERM [29], the marker trajectories can violate conservation principles and cross physically impermeable boundaries. Moreover, in the case where the time step is too large, due to time integration of marker trajectories (Runge-Kutta scheme), a marker can cross an impenetrable physical boundary (marker 4 in Fig. 3). These later markers are simply deactivated during the position update (Eqs. (7) and/or (9)).

Scalar conditions

For solid walls, the most used boundary conditions are homogeneous Dirichlet or Neumann conditions. As mentioned above, the Eulerian boundary conditions are implicitly imposed

during the diffusion process with a volume penalty method [22] adapted for scalar equations. It consists in the addition of a penalty term $B\left(f(\Phi)-\gamma\right)$ in the conservation equation, such that the unsteady diffusion equation can be formally rewritten, with a first-order time discretization, as

$$\frac{\Phi^{n+1}-\Phi^{n}}{\Delta t}-\vec{\nabla}\cdot\left(\Gamma\vec{\nabla}\Phi^{n+1}\right)-B\left(f(\Phi^{n+1})-\gamma\right)=0 \tag{13}$$

where B is the penalty coefficient and γ the value of variable Φ or its derivative to be imposed on the given boundary. If $B\to 0$, the classic diffusion equation is obtained while if $B\to\infty$, $f(\Phi^{n+1})$ takes the imposed value γ. The definition of function f then specifies the kind of boundary condition that is applied by penalty. It is more convenient to specify the f function once the space discretization is made. In the general case, with the boundary condition applied on the ijk node, the penalty term is finally approximated by

$$\begin{aligned}B\left(f(\Phi^{n+1})-\gamma\right)\simeq B_{i,j,k}\Bigg[&\alpha_{i,j,k}\Phi^{n+1}_{i,j,k}\\&+\beta^{(x)}_{i,j,k}\frac{\Phi^{n+1}_{i+1,j,k}-\Phi^{n+1}_{i-1,j,k}}{2\Delta x}\\&+\beta^{(y)}_{i,j,k}\frac{\Phi^{n+1}_{i,j+1,k}-\Phi^{n+1}_{i,j-1,k}}{2\Delta y}\\&+\beta^{(z)}_{i,j,k}\frac{\Phi^{n+1}_{i,j,k+1}-\Phi^{n+1}_{i,j,k-1}}{2\Delta z}\\&-\gamma_{i,j,k}\Bigg]\end{aligned} \tag{14}$$

where $\alpha_{i,j,k}$ and $\beta^{(\bullet)}_{i,j,k}$ are coefficients allowing to locally achieve Dirichlet ($\alpha_{i,j,k}=1$ and $\beta^{(\bullet)}_{i,j,k}=0$), Neumann ($\alpha_{i,j,k}=0$ and $\beta^{(\bullet)}_{i,j,k}=1$) or mixed ($\alpha_{i,j,k}\neq 0$ and $\beta^{(\bullet)}_{i,j,k}\neq 0$) boundary conditions ($\bullet=x$, y or z denotes the direction to which the boundary condition is applied). The coefficients β carry the information of the direction to which gradient $\vec{\nabla}\phi$ is oriented (i.e., a Neumann condition like $\vec{\nabla}\phi\cdot\vec{n}=\gamma$). Note that the interest of this formulation is that it allows for imposing immersed boundary conditions in cells not belonging to physical boundary conditions. Practically, the penalty coefficient is set to $B_{i,j,k}=10^{40}$ at boundary scalar nodes and left to $B_{i,j,k}=0$ elsewhere in the fluid domain.

Without any specific treatment, the boundary conditions of the continuum problem are not satisfied by the MEL approach. The update of ϕ values (Eq. (11)) is then modified for activated markers in scalar boundary cells (empty blue diamonds indexed from 1 to 3 in Fig. 3). The main idea is that the averaged value computed from marker information on a scalar boundary cell is expected to satisfy the prescribed conditions. In the method developed here, the boundary conditions are implicitly imposed on the Eulerian field during the diffusion process (Eqs. (3) or (13), line 20 of Algorithm 1). The Φ^{n+1} value after this step then satisfies boundary conditions, regardless of their type. A simple way to convey this information to the markers is then to replace Eq. (11) by

$$\phi^{n+1}_{m}=\Phi^{n+1}_{i,j,k} \tag{15}$$

at boundary scalar cells.

Note that in the case of a fluid flow output, for example with zero gradient condition on the velocity normal component, the particles that go outside the computational domain undergo the following treatment: i) the average computation (Eq. (10)) allows building a post-advection value on the boundary scalar nodes; ii) the marker is deactivated or reused at an inlet condition (the carried value ϕ is changed according to the case).

3 Results

AAAAAAAAAAAAAAAAAAAAAAAAAA

The proposed Mixed Eulerian-Lagrangian approach for Advection Diffusion Equation is developed from the VSM scheme [42] that was initially devoted to advection equation only. One-dimensional cases and convergence analysis of the transport of various functions can be found in [42]. Adding the diffusive contribution, the MEL method is first tested in a one-dimensional configuration.

In a periodic domain defined by $x \in [-L/2, L/2]$, $L = 1$ m, a peak of concentration of half-length $\ell_0/L = 1$ is placed at $x = 0$. With a constant velocity field, $u = 1$ m/s, the peak center returns to its initial position after 1 second. The concentration peak is smoothed according to the diffusion coefficient value. The analytical solution is given in Appendix A.1 by Eq. (28).

Figure 4 presents, for different space steps, the solutions for two values of the diffusivity Γ. Only few nodes, around 10, are necessary over the peak length to recover the solution. It has

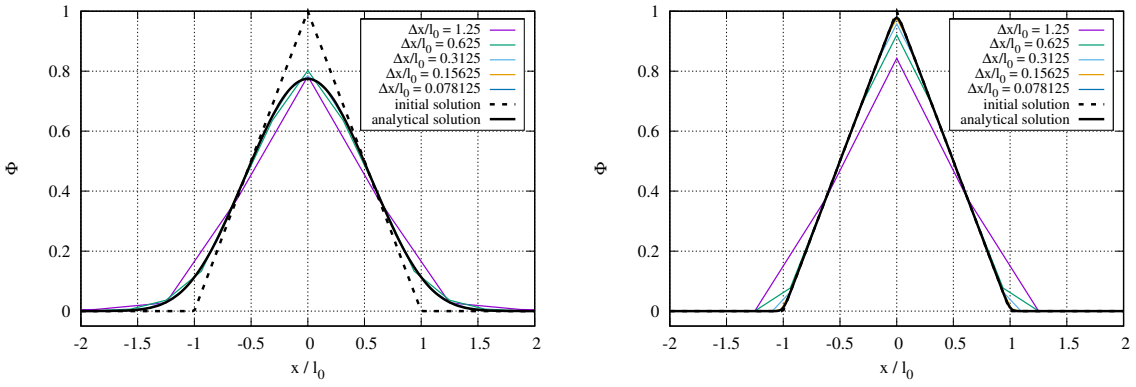

(a) $\Gamma = 10^{-4}$ m^2/s

(b) $\Gamma = 10^{-6}$ m^2/s

Figure 4: Analytical solution at $t = 1$ and numerical profiles obtained with the MEL scheme for different space steps and two values of Γ. The dashed line shows the initial condition.

been checked that the solution converges to the analytical one with a second order accuracy. However, this test case is not enough discriminatory. Indeed, as the velocity is constant, both the interpolation at marker positions and the time integration with a RK scheme are exact, regardless of the value of the CFL condition. In fact, a time step based on the maximum CFL value, i.e., $u\Delta t/L$, allows to recover the solution. Moreover, as each marker moves with the same velocity, all cells contain, for each time step, the same number of particles which makes the reseeding procedures not necessary. Finally, the particle density number P, does not have a significant influence on the solution or the order of accuracy. In this specific configuration,

the MEL approach is more accurate and efficient than any other Eulerian scheme (except the explicit upwind scheme with CFL = 1). As this 1D configuration avoids the complexity of scalar transport in real cases, the Mixed Eulerian-Lagrangian scheme will be tested in 2D and 3D situations with given velocity fields before an application to a natural convection case involving a coupling with the Navier-Stokes equations.

3.1 Advection-diffusion of a concentration peak

The case is a two-dimensional extension of the configuration above introduced. Simple to implement, it makes spatial interpolations and time integrations no longer trivial. Reseeding procedure is also required.

3.1.1 Problem setup

A peak of concentration is placed in a square domain defined by $(x, y) \in [0, L]^2$, $L = 1$ m, with the velocity field expressed as

$$\vec{u}(x, y) = u\vec{e}_x + v\vec{e}_y = \frac{\pi}{2}\begin{pmatrix} -(y - y_c) \\ x - x_c \end{pmatrix} \tag{16}$$

A solid body rotation motion is generated around the fixed point $(x_c, y_c) = (L/2, L/2)$. A marker placed in this field needs $t = 4$ seconds to make a complete turn and return to its initial position. In this analytical velocity field, a peak of concentration (dimensionless volume fraction) of radius $r_0 = L/10$ is initialized such as

$$\Phi(r, t = 0) = \begin{cases} \dfrac{r_0 - r}{r_0} & \text{if } r \leq r_0 \\ 0 & \text{otherwise} \end{cases} \tag{17}$$

where $r = \sqrt{(x - x_p)^2 + (y - y_p)^2}$ is the radial coordinate centered around (x_p, y_p) the position of the peak center. At initial time, $(x_p, y_p) = (L/2, 3L/4)$. The reference solution over time in the moving frame of the concentration peak is given by

$$\Phi_{ref}(r, t) = \sum_{n=1}^{\infty} A_n J_0(\lambda_n r) \exp(-\lambda_n^2 \Gamma t) \tag{18}$$

where J_0 is the zeroth order Bessel function of the first kind and $\lambda_n r_0$ the n^{th} root of $J_0(x) = 0$. The expression of coefficient A_n is given in Appendix A.2 by Eq. (45). Practically, the first 200 terms are used to compute the reference solution given by Eq. (18). The numerical solutions obtained with different schemes are compared to this reference solution after a simulation time of $t = 4$ seconds (corresponding to 1 turn), and the diffusion coefficient Γ varies from 10^{-4} to 10^{-6} m^2/s.

Snapshots of the reference solution Φ_{ref} are presented in Fig. 5 for different times. The z-axis and iso-values $\Phi = 0.01$, 0.1, 0.5 and 0.9 are used to represent the intensity of the concentration peak. After one turn, the peak is diffused around its initial position according to the diffusion coefficient $\Gamma = 10^{-4}$ m^2/s.

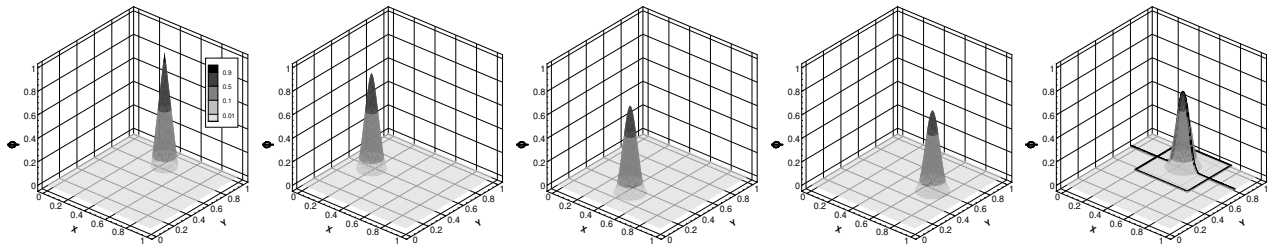

(a) $t = 0$ s (b) $t = 1$ s (c) $t = 2$ s (d) $t = 3$ s (e) $t = 4$ s

Figure 5: Reference solution for times $t = 0$, 1, 2, 3 and 4 s and for $\Gamma = 10^{-4}$. Iso-values are 0.9, 0.5, 0.1 and 0.01. Square and dot-dashed line presented in Fig. 5(e) show the zones in which the solution presented in the next section.

The diffusion scale δ is defined through the analytical solution by $\Phi(\delta, t) = \Phi_\infty + 1\%\Delta\Phi$ where $\Phi_\infty = 0$ and $\Delta\Phi = 1$ are, respectively, the concentration far from the peak and the maximum concentration difference. The computed constant of Eq. (4) is then $K \approx 2.2$ and leads to η values of about 100 to 1000, respectively, for $\Gamma = 10^{-4}$ and 10^{-6} m^2/s. The choice of the diffusivity Γ has been motivated by allowing for a noticeable diffusion after one turn of the peak while keeping its initial shape almost unchanged, so as to try to keep the sharp profile of it. This is equivalent to have a high Péclet number. In the present configuration, based on the initial peak diameter and velocity, $Pe = 785$ and 78500, respectively, with $\Gamma = 10^{-4}$ and 10^{-6} m^2/s. The domain is first discretized with $N_x = N_y = N$ regular control volumes in each space direction and the time step Δt is chosen according to CFL condition defined by $\frac{\pi}{4}\Delta t/\Delta x$ ($\pi/4$ is the maximum velocity).

3.1.2 Convergence study and computational cost

A first set of results is shown in Fig. 6 for $\Gamma = 10^{-4}$ and 10^{-6} m^2/s and different schemes. Four concentration iso-values ($\Phi = 0.9$, 0.5, 0.1 and 0.01) obtained from numerical simulation are plotted and compared to the reference one. As mentioned above, due to the high value of the Péclet number, the centered scheme is unstable and the low order upwind scheme is very diffusive (almost 85% of the signal is lost after one turn). The MUSCL and QUICK schemes have also been tested. They give very similar results and present an excessive numerical diffusion in the fluid flow direction (not presented). Finally, the Lax-Wendroff TVD, WENO5 and MEL schemes give the best results (WENO5n and WENO5c stand, respectively, for non-conservative and conservative WENO5 schemes). For $\Gamma = 10^{-4}$ m^2/s, the Lax-Wendroff scheme is anti-diffusive and then tends to stiffen the signal, while WENO5 schemes give accurate solutions. The MEL method, used here with the particle density number $P = 2$, also gives a good solution but introduces oscillations in the solution. For a smaller diffusion coefficient, $\Gamma = 10^{-6}$ m^2/s, the WENO5 schemes introduce more diffusion. Oscillations still slightly disrupt the numerical solution of the MEL approach. However, this later does not introduce numerical diffusion and presents, on this mesh, a better solution than Lax-Wendroff and WENO5 schemes. Note that the MEL, with $P = 2$ particles per direction and per cell, is able to represent 95% of the peak value.

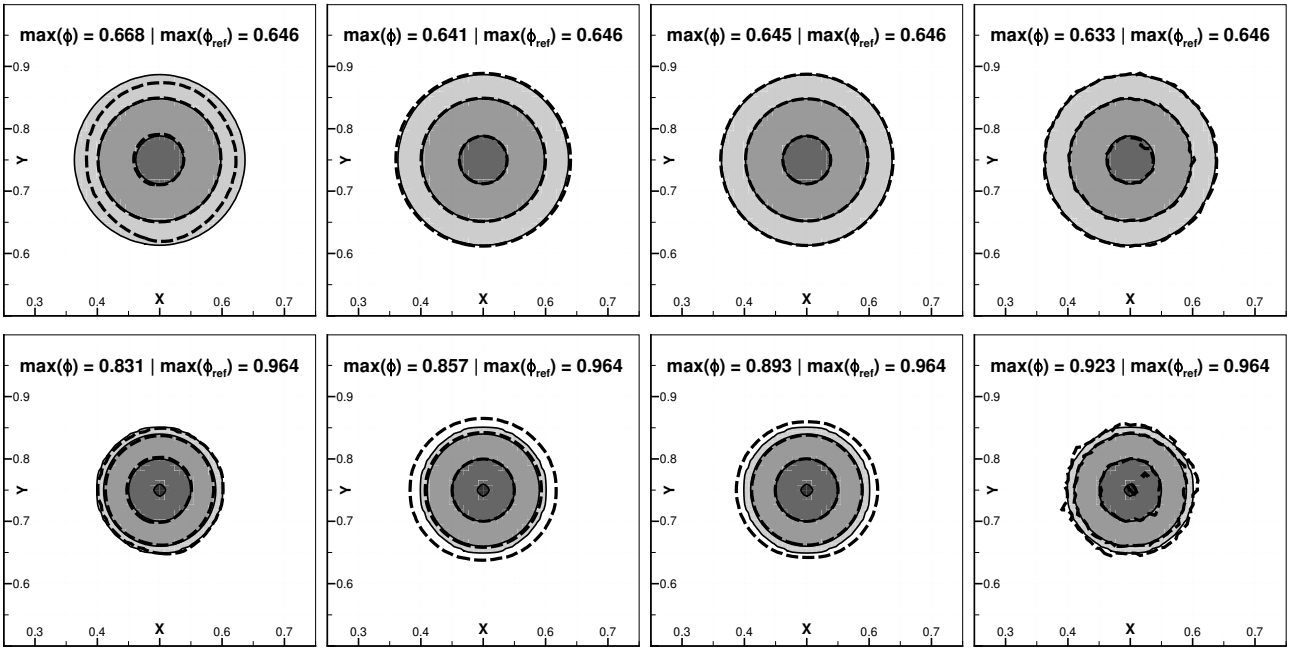

(a) Lax-Wendroff TVD (b) WENO5n (c) WENO5c (d) MEL

Figure 6: Zoom on the numerical (black dashed lines) and reference solutions (filled) after one turn for different schemes on a $N^2 = 128^2$ mesh and for $\Gamma = 10^{-4}$ (top row) and $\Gamma = 10^{-6}$ m^2/s (bottom row). The CFL is set to 0.5. Iso-lines are, starting from the peak center, equal to 0.9, 0.5, 0.1 and 0.01 (iso-line 0.9 is not present for $\Gamma = 10^{-4}$ m^2/s).

The second set of results (Fig. 7) presents, on the same mesh, the solutions obtained with the MEL scheme and different values of the particle density number P. The first observation is that the oscillations can be reduced by increasing P. At the same time, the quality of the solution increases; 99.2% of the peak value is correctly represented for $P = 8$. It has been verified that the oscillations come from the reseeding procedures. Indeed, all the markers follow circle trajectories and come back to their initial position after time $t = 4$ s. Removing reseeding procedures in this particular rotation motion case suppresses the oscillations even with a small particle density number value. However, in practical cases, enrichment is mandatory to balance particle lack in sheared zones. Furthermore, it has been checked that, for a defined case, different simulation runs associated with different random draws (used in the particles reseeding procedures) lead to various solutions around the expected statistical solution.

As the projection of the Eulerian field on Lagrangian markers is made with an interpolation and its opposite with an average, nothing guarantees the conservation of the global scheme. In practice, we use the volume brought by the markers to transfer the Lagrangian information to the Eulerian grid, i.e., the estimation of the Eulerian concentration or temperature. At the opposite, when the Eulerian scalar information is transferred from the Eulerian mesh to the markers, the volume brought by the markers is not considered in the present version of the paper. This step aims to ensure local conservation (on the Eulerian cell) of the given quantity but not the global one. In order to illustrate the reseeding procedures effect on the global

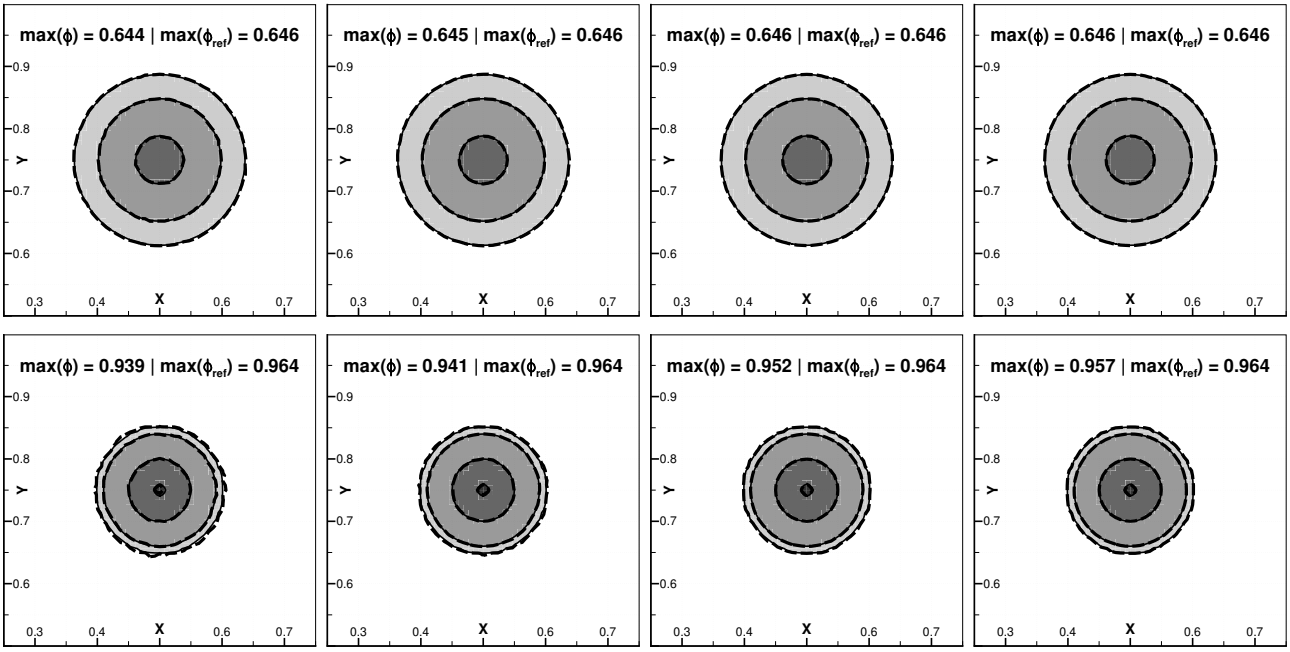

(a) $P = 3$ (b) $P = 4$ (c) $P = 6$ (d) $P = 8$

Figure 7: Zoom on the numerical (black dashed lines) and reference solutions (filled) after one turn for different values of P on a $N^2 = 128^2$ mesh and for $\Gamma = 10^{-4}$ (top row) and $\Gamma = 10^{-6}$ m^2/s (bottom row). The CFL is set to 0.5. Same iso-lines as in Fig. 6 are shown.

conservation, the quantity

$$err_C(t) = \frac{1}{N_R} \sum_{i}^{N_R} \frac{\displaystyle\int_D \Phi(t; x, y)\, dS}{\displaystyle\int_D \Phi(t = 0; x, y)\, dS} - 1 \tag{19}$$

which represents the relative variation of the integral of Φ over the whole domain, averaged on N_R different runs, is plotted in Fig. 8 for different meshes and the particle density number $P = 4$. In the case of a conservative scheme, for example for the conservative WENO5 scheme (not shown), the value of err_C is strictly 0 over time.

For the coarse $N^2 = 32^2$ mesh, the error oscillates over a range of 10%. Although the average conservation is quite similar to the two times smaller $N^2 = 64^2$ mesh, the amplitude of oscillations shows that the solution is less accurate. Both the variation range and the oscillations are significantly reduced increasing the resolution. On the chosen mesh for illustration and comparisons, $N^2 = 128^2$, the quantity Φ is conserved with a relative error lower than 0.5‰ in relation to the initial value. The errors are insensitive with the diffusion coefficient value. It is worth mentioning that the quantity err_C only gives information about the conservation but not on the solution. For example, the upwind scheme is conservative but (very) diffusive. In this case, err_C will be 0, but the solution will be far away from the expected one, as presented in the following.

Figure 9 synthesizes the previous results with plots of the concentration values on the line defined by $y = 3L/4$ and after one turn. For the diffusivity $\Gamma = 10^{-4}$ m^2/s (Fig. 9(a)) and at the plotting scale, the analytical solution is superposed to the WENO5 and MEL scheme solutions.

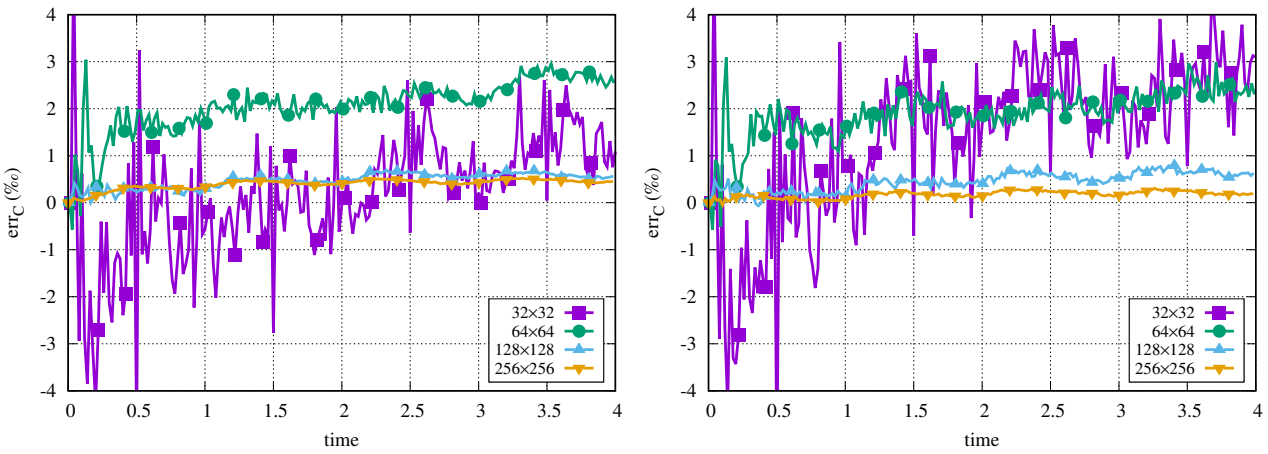

(a) $\Gamma = 10^{-4}$ m^2/s (b) $\Gamma = 10^{-6}$ m^2/s

Figure 8: Evolution of the global conservation estimator err_C over time for different meshes. The averages are done over $N_R = 128$ runs. (A study on the mean value and variance has been performed on the 64^2 mesh and over 2048 runs and has shown a convergence around the $N_R = 128$ value.)

As mentioned above, the Lax-Wendroff TVD scheme amplifies the stiffness of the concentration profile; the solution overestimates the maximum value. The case with the low diffusivity value $\Gamma = 10^{-6}$ m^2/s (Fig. 9(b)) allows a better discrimination against the different schemes. Only the MEL approach is able to properly reproduce the concentration profile. The oscillations are strongly reduced and are no longer distinguishable at the figure scale, as soon as the particle density number $P > 2$. All the other tested schemes introduce a significant numerical diffusion and deviate from the analytical solution. In the class of Eulerian approaches, the conservative version of the WENO5 scheme is identified as the best for this problem. Centered and upwind implicit schemes are also given for guidance purposes. Note that contrary to the explicit version, the centered scheme is not dispersive and allows to obtain a solution. For the presented range of x-positions, oscillations of the centered scheme are not visible, but the global solution provides undershoots of about 5% of the maximum value.

Figure 10 presents the space convergence of the relative error defined by

$$err = \left(\frac{\int_0^L \int_0^L (\Phi - \Phi_{ref})^2 \, dxdy}{\int_0^L \int_0^L \Phi_{ref}^2 \, dxdy} \right)^{\frac{1}{2}} \tag{20}$$

between simulation and reference solutions after one turn and for $\Gamma = 10^{-4}$ and 10^{-6} m^2/s. Generally, and as mentioned above, the WENO5c scheme is more accurate than the WENO5n and Lax-Wendroff schemes. Its convergence order is strongly linked to the regularity of the solution. For $\Gamma = 10^{-4}$ m^2/s, the diffusion process quickly smooths the initial piecewise concentration peak and a third order convergence is observed (it has been checked that the theoretical fifth order convergence is obtained for regular functions such as sinusoidal profiles). In the case of a lower diffusivity, $\Gamma = 10^{-6}$ m^2/s, the Lax-Wendroff and WENO5 schemes present quite similar convergence orders that tend toward second order accuracy in the asymptotic region. Again,

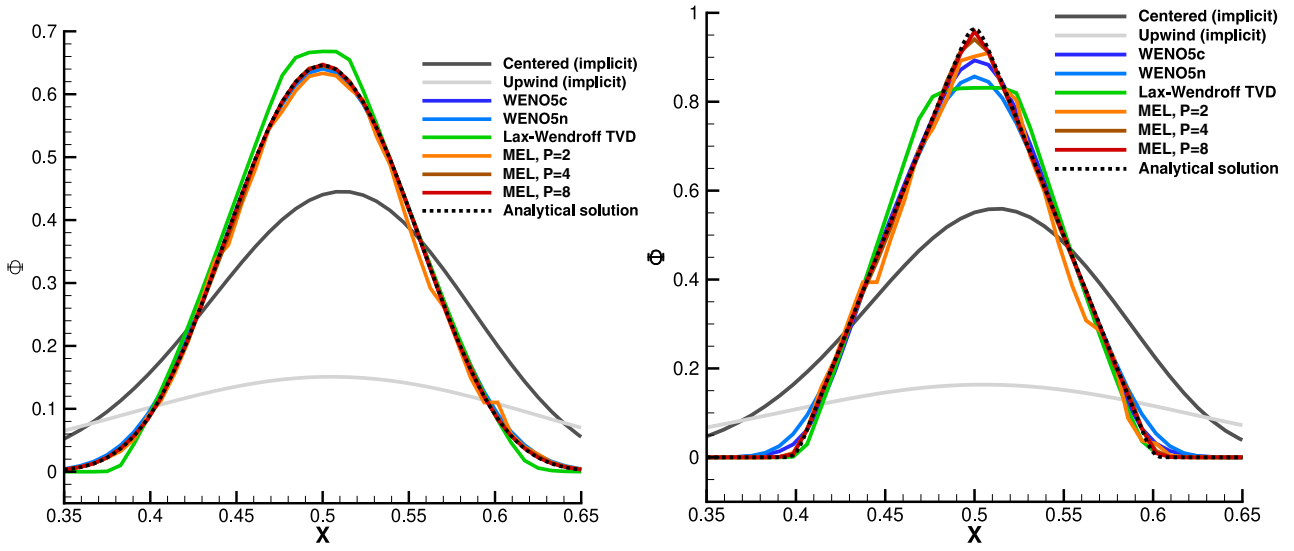

(a) $\Gamma = 10^{-4}$ m^2/s (b) $\Gamma = 10^{-6}$ m^2/s

Figure 9: Solution profiles on the line $y = 3L/4$ after one turn for the different schemes on a $N^2 = 128^2$ mesh and two values of Γ. The CFL is set to 0.5.

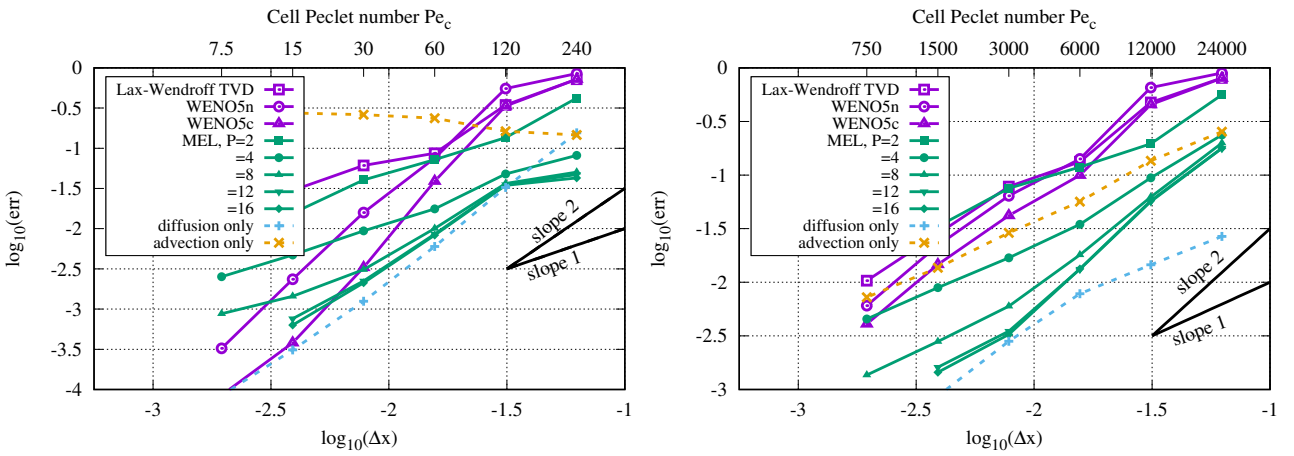

(a) $\Gamma = 10^{-4}$ m^2/s (b) $\Gamma = 10^{-6}$ m^2/s

Figure 10: Evolution of error with the space step with $\Delta x = 1/N$, $N = 16$ (most right points), $32, \ldots, 512$ for different diffusivity values. The CFL condition is kept at 0.5. For guidance, the top horizontal axis gives the cell Péclet number Pe_c.

among the cited schemes, WENO5c gives the best results and is used for comparisons with the MEL scheme in the rest of this paper.

The convergence order and level of accuracy of the MEL method are strongly linked to the particle density number value P but also to the diffusivity Γ. Figure 10 shows that for given mesh and P, the error level is smaller for a larger diffusion coefficient. Nevertheless, this variation is small for two orders of magnitude of the diffusion coefficient compared to the order of magnitude of error when acting on P. The scheme is then less adapted to cases involving ratio η of about the unity or less. Obviously, in these cases, classical centered or upwind schemes will give better results for shorter computing times (compared to WENO5 or MEL). For a particle density number $P = 2$ and despite the numerical oscillations observed on the solution, the error

level is quite similar to the Lax-Wendroff scheme and the slope suggests a first order accuracy. Increasing P significantly reduces the error level and increases the accuracy order to about 2 for $P = 16$. Furthermore, increasing P is also useless beyond a certain value (here 12) and the increased accuracy is negligible compared to the additional computational cost. Finally, as a practical result, the convergence results show that for low diffusivity $\Gamma = 10^{-6}$ m^2/s and on a 128^2 mesh, the error level of the MEL is about one order of magnitude lower than the WENO5c scheme as soon as the particle density number $P \geq 8$. Note that the same accuracy level can be reached with the WENO5c scheme for four times finer meshes. Even for intermediate values of P between 2 and 8, the MEL gives more accurate results on coarser grids than WENO5c.

For the analysis, the errors associated with the pure advection (solving only Eq. (2) with the Lagrangian scheme) and pure diffusion (Eq. (3)) cases are added. As the analytical solution is purely diffusive in the moving reference frame, the associated error obtained for this last case is only linked with the accuracy to the diffusion solver. For a smooth solution, (like in Fig. 9(a)), a second order accuracy is obtained, while in the case of a stiffer case (Fig. 9(b)), the second order is only reached in the asymptotic region; a first order accuracy is obtained on coarse meshes. The error considering only the advection part is large when the diffusion coefficient is high. On the other hand, one might think that solving only advection in such heavily advection-dominated problem might be sufficient. This is indeed the case if we compare the error made with that of the Eulerian schemes. On the contrary, the figure clearly shows the profit related to the MEL approach: the error is bounded by the advective and diffusive solutions, and, even for small diffusion values, the consideration of the diffusion reduces the error by one or two orders of magnitude depending on the particle density number value P.

Finally, the number of particles per direction and per cell P can be regarded as a discretization parameter. A convergence with this parameter is presented in Fig 11. The errors decrease

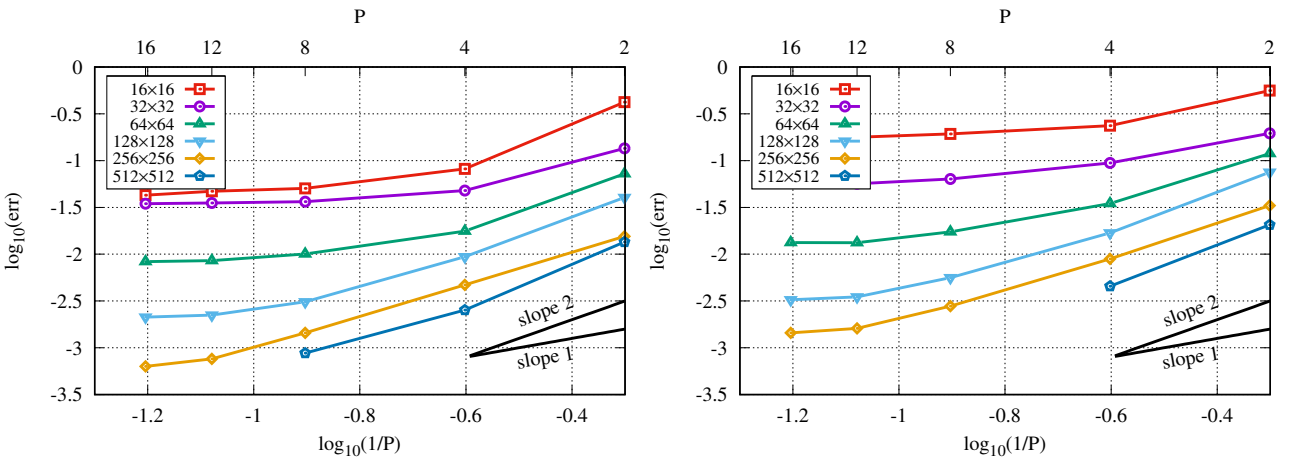

(a) $\Gamma = 10^{-4}$ m^2/s (b) $\Gamma = 10^{-6}$ m^2/s

Figure 11: Evolution of error with $1/P$, $P = 2$ (most right points), $4, 8, 12, 16$ for different diffusivity values. The CFL condition is kept at 0.5.

with the number of particles per cell. The slopes suggest a second order variation up to P values around 4 and 8. A first order is obtained for intermediate values between 8 and 12, while a constant value is reached for $P \gtrsim 12$. An optimal parameter is between 4 and 8 and

must be chosen according to the CPU time cost of the computation as discussed in the next paragraph.

As the Lagrangian particle tracking has an extra computational time (increasing with the particle number), this later must be included in the analyses. Figure 12 shows the computational cost for the different approaches, always for two Γ values. All the costs are normalized by the

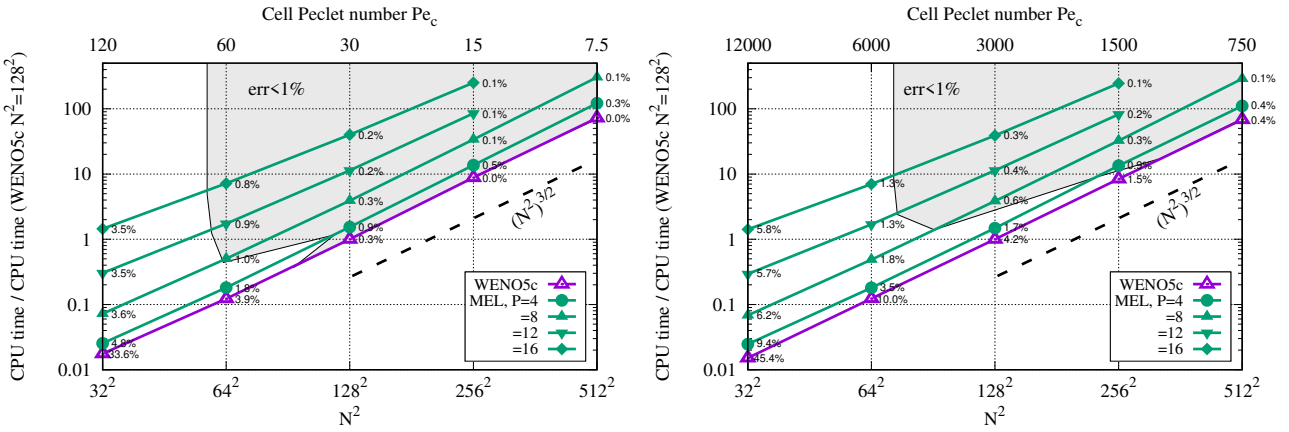

(a) $\Gamma = 10^{-4}$ m^2/s (b) $\Gamma = 10^{-6}$ m^2/s

Figure 12: Normalized computational cost for the different schemes as a function of the total unknowns N^2. The gray area represents solutions with less than 1% relative difference (numerical values) with the reference solution.

simulation time with the WENO5c scheme on a 128^2 mesh. First, the cost increases as N^3 for all schemes. In the case of the MEL scheme, increasing the number of particles per direction and per cell P obviously increases the computational cost. For the reference mesh 128^3, the extra cost is 50% for the particle density number $P = 4$, but it is multiplied by a factor 4 for $P = 8$ and by 11 for $P = 12$. Note that according to the convergence study, it is not interesting to increase P beyond a value around 12. The numerical values associated with each point stand for the relative error to the reference solution. The gray area in Fig. 12 represents the solution with less than 1% difference from the reference. It has been reconstructed by approximating the meshes leading to 1% error from the convergence study presented in Fig. 10. This 1% zone is lower bounded by the WENO5c scheme and left bounded by the minimal mesh necessary to obtain a 1% accurate solution. From these figures, it can be extracted that:

- The analysis of the 1% area associated with considering only the MEL scheme exhibits an optimal value of 8 for the particle density number P.
- The MEL approach is quite insensitive to the ratio η between advection and diffusion. With meshes around 100^2 and increasing the particle density number P, it is possible to obtain an accurate solution (here 1% error from the reference). The slight increase in the minimal required mesh is driven by the diffusion process.
- However, for small η ratio, the setup of the MEL method is not justified since it introduces a non negligible extra cost of about 25% compared to the simulation with the WENO5c

scheme on finer grid. For example, from Fig. 12(a), 1% error solution is obtained on a 64^2 mesh and $P = 8$ for MEL and a normalized computation time of about 0.5, while extrapolation shows that an equivalent solution can be obtained with the WENO5c scheme on a mesh of about 100^2 for a normalized computation time of about 0.4.

- For large η ratio, the computation cost is totally reversed as the required meshes are very different. The MEL method needs a mesh of about $N^2 = 90^2$ and a particle density number $P = 8$ while the WENO5c scheme reaches the same accuracy on a 320^2 mesh (Fig. 12(b)). The Lagrangian approach allows three times coarser grids than classical schemes. The ratio of CPU times is then strongly affected: the MEL scheme is at least one order of magnitude cheaper (or faster) than WENO5c.

In practice, the particle density number value $P = 4$ is chosen. Through the different examples discussed, this value is the best compromise between the CPU cost and the accuracy. Just as one does space and time convergences in order to find proper values of space and time steps, a convergence study (see for example [42]) can be investigated to optimize the value of P.

3.2 Concentration spot in a sheared field

To illustrate the capacity of the Mixed Eulerian-Lagrangian scheme to approximate a physical field even on coarse meshes, a spot of concentration

$$\Phi(r, t = 0) = \begin{cases} 1 & \text{if } r \leq r_0 \\ 0 & \text{otherwise} \end{cases} \tag{21}$$

is now advected in a sheared incompressible flow field given by

$$\vec{u}(x, y) = \frac{\pi}{2} \begin{pmatrix} -\sin^2(\pi x)\cos(\pi y)\sin(\pi y) \\ \sin^2(\pi y)\cos(\pi x)\sin(\pi x) \end{pmatrix} \tag{22}$$

in the domain $[0, L]^2$, $L = 1$ m. The solutions are presented for $t = 4$ seconds for the MEL scheme with the particle density number $P = 4$, the WENO5c and the centered schemes. Two regular grids are used, a "coarse" 128^2 mesh and a four time finer 512^2 mesh. The diffusion coefficient varies form $\Gamma = 10^{-4}$ to 10^{-6} m^2/s. Magnitude orders of η and Péclet number are the same as in the previous section. Results are plotted in Fig. 13.

- For high diffusion value (top line), all schemes on the fine mesh give very similar results. On the coarse mesh, the MEL scheme with $P = 4$ particles per direction and per cell presents a good solution, while the WENO5c scheme is not able to represent high values of the concentration field.

- For lower values of the diffusion coefficient, on the coarser mesh, the WENO5c is no more able to discriminate against the diffusion process. The results are improved on the finer mesh but remain too much diffusive. Concerning the centered scheme, it provides results comparable to the WENO5c scheme except for the lower diffusion coefficient. In all cases and for all meshes, the MEL scheme provides a more accurate solution that is able to

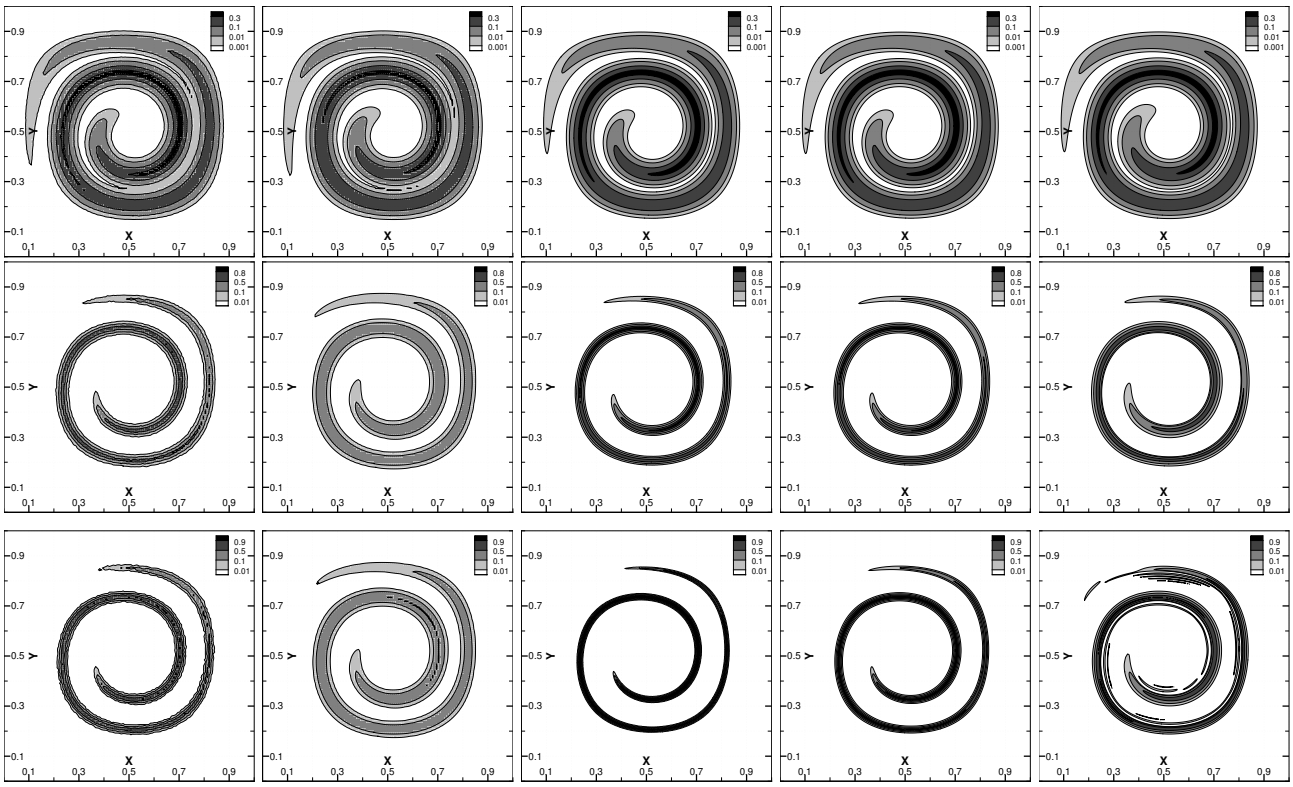

(a) MEL, 128^2 (b) WENO5c, 128^2 (c) MEL, 512^2 (d) WENO5c, 512^2 (e) Centered, 512^2

Figure 13: Iso-lines of concentration at $t = 4$ s. From top to bottom $\Gamma = 10^{-4}$, 10^{-5} and 10^{-6} m^2/s. The centered scheme (last column) is presented as guidance for the finer mesh. It introduces oscillations for high values of the Péclet cell number, here for coarse meshes (not presented) or a low Γ value.

account for diffusion, even when advection is predominant. The coarse MEL solution is comparable to the 512^2 solutions brought by the Eulerian schemes. This is a very nice feature and advantage of the MEL approach.

The maximum concentration values at $t = 4$ s are summarized in Tab. 1 for different meshes. As shown in Sect. 3.1.1 in a similar situation, the MEL scheme produces the lower error level; its

N^2	32^2		64^2		128^2		256^2		512^2	
Γ (m^2/s)	MEL, $P = 4$									
10^{-4}	0.455	(22%)	0.412	(11%)	0.382	(3%)	0.372	(0.3%)	0.371	(ref.)
10^{-5}	0.559	(-35%)	0.740	(-14%)	0.821	(-6%)	0.854	(-2%)	0.869	(ref.)
10^{-6}	0.506	(-50%)	0.770	(-22%)	0.956	(-4%)	0.990	(-1%)	0.998	(ref.)
	WENO5c									
10^{-4}	0.170	(-54%)	0.254	(-31%)	0.344	(-7%)	0.370	(-0.3%)	0.371	(0%)
10^{-5}	0.179	(-79%)	0.290	(-66%)	0.496	(-43%)	0.760	(-13%)	0.864	(-0.5%)
10^{-6}	0.180	(-81%)	0.294	(-70%)	0.516	(-48%)	0.864	(-13%)	1.020	(2%)

Table 1: Convergence of $\max(\Phi(t = 4\,\text{s}))$ with the grid for different diffusion coefficient values and for MEL and WENO5c schemes. Results with MEL scheme on the 512^2 mesh serves as reference. The bracketed values stand for the relative difference with the reference.

results on the finer mesh are then used as reference. In the range of covered diffusion coefficient, leading to Péclet numbers from about 10^3 to 10^5, both schemes converge through similar values. On the finer grid, the relative difference between MEL and WENO5c increases as the diffusion coefficient decreases. For $\Gamma = 10^{-6}$ m^2/s, an over-estimated value (above the upper bound $\Phi = 1$) occurs for the WENO5c scheme and produces a maximum difference around 2%.

Except the MEL approach with $\Gamma = 10^{-4}$ m^2/s, the maximum value max(Φ) converges by lower values to the reference. The over-estimated values with the MEL scheme are very localized and are explained by the reseeding procedures (see Sect. 2). In the same way as in Sect. 3.1.2, the results show that a finer grid is needed by the WENO5c scheme in order to reach the same level of error as the MEL. As only the velocity field changes, the computational costs are similar to those presented in Fig. 12, which makes the Mixed Eulerian-Lagrangian scheme more efficient to reach a fixed level of accuracy. In this case, around $N^2 = 128^2$ grid points are required to reach an error around 5% with the MEL, while WENO5c needs more than a 256^2 mesh. To obtain the same level of accuracy, the CPU time ratio between the MEL and the WENO5c schemes is approximately 1/5.

3.3 Three-dimensional deformation

The approach is now applied in a three-dimensional configuration. As in the previous section, schemes are compared on coarse grids and a four time finer mesh is used to compute a reference. The underlying idea is that in CFD simulations dealing with passive scalar, the grid choice is generally based on convergence of the velocity field. Here, the purpose of the 3D simulations is to illustrate the capability of Mixed Eulerian-Lagrangian scheme to deal with sharp concentration profiles at high Péclet numbers (or η values). The aim is to be able to undertake these cases with relatively coarse grids compared to classical Eulerian methods dealing with the hyperbolic advection term, like WENO or TVD schemes.

In a box unit, the incompressible flow field is given by [26]:

$$\vec{u}(x,y,z) = \begin{pmatrix} 2\sin^2(\pi x)\sin(2\pi y)\sin(2\pi z) \\ -\sin(2\pi x)\sin^2(\pi y)\sin(2\pi z) \\ -\sin(2\pi x)\sin(2\pi y)\sin^2(\pi z) \end{pmatrix} \tag{23}$$

In the constant field $\Phi = 0$ of diffusivity $\Gamma = 10^{-6}$, a sphere of radius 0.15 m and reduced concentration $\Phi = 1$ is placed at $(x, y, z) = (0.35\,\text{m}, 0.35\,\text{m}, 0.35\,\text{m})$. Its evolution is simulated over one second, and final iso-surfaces of concentration $\Phi = 0.2$ and 0.9 are plotted in Fig. 14

As explained in [11], this test case shows some surface aliasing when the resolution is insufficient to resolve thin filaments, or films, formed during the simulation. The WENO5c simulation on a 256^3 mesh (Fig. 14(d)) is used as a reference. Comparisons with schemes on four time coarser grids show a good overall agreement except for the restitution of the filament whose thickness is of the order of the space step. On the same 64^3 mesh, the WENO5c scheme (Fig. 14(a)) loses a large part of the film that the MEL approach is almost able to render totally, whatever the spatial interpolation method used (classical Q1 or high level interpolation method PERM [29]). Differences are also observed on high values of the concentration, here

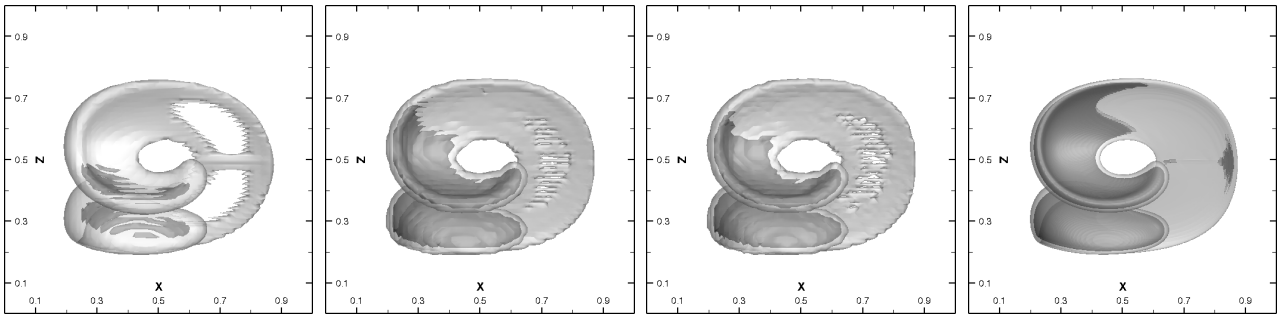

(a) WENO5c, 64^3 (b) MEL/Q1, 64^3 (c) MEL/PERM, 64^3 (d) WENO5c, 256^3

Figure 14: XZ view of iso-surfaces $\Phi = 0.2$ (gray) and 0.9 (dark gray) for schemes (a) WENO5c on a 64^3 mesh, MEL with the particle density number $P = 4$ on 64^3 meshes for Q1 (b) and PERM (c) spatial interpolations and (d) WENO5c on a 256^3 mesh, which is used as a reference. The time is $t = 1$ second, the diffusivity is $\Gamma = 10^{-6}$ m^2/s and the CFL $= 0.5$.

$\Phi \geq 0.9$. Again, the non-diffusive nature of the advection term in the MEL method allows a better representation of the passive scalar physics on meshes for which the velocity field is well resolved but which would require two to three times more cells per direction when classical Eulerian schemes are used.

In this paper, no effort has been made to optimize the computational extra cost of the Mixed Eulerian-Lagrangian scheme. As the particle density number P is the same per direction, each cell contains P^3 particles and the additional cost arising by using one more particle per direction is important to consider as well as the memory requirements. Particle number optimization strategies, e.g., by making the number of markers per cell independent of the spatial dimension d or local adaptations of P in each cell, in a kind of AMR approach for MEL scheme, according to the Φ variations are currently being developed. First, results show that they allow to significantly reduce the computational cost of the MEL scheme.

3.4 Natural convection

The mixed Eulerian-Lagrangian scheme is now applied to the very used benchmark case of the thermally driven square cavity. The scalar Φ here represents the temperature field T. The Navier-Stokes and energy equations are coupled through the Boussinesq assumption for the volume forces in the y-momentum contribution. The Rayleigh Ra and Prandtl Pr numbers are the dimensionless parameters of interest for this study. The attention is focused on the $Pr = 0.71$ and $Ra = 10^6$ configuration.

The difficulty of this case is to have sufficiently fine meshes near walls in order to correctly represent the dynamical and thermal boundary layers whose thicknesses decrease with the Rayleigh number. To this purpose, spectral methods, based on global approximation of spatial derivatives, need approximately four times less nodes than Finite-Volume method (see for example [6] and [25]). They then provide accurate values for comparison purposes. Several characteristic values, obtained for Gauss-Lobatto distribution of cell centers, with the centered and the Mixed Eulerian-Lagrangian schemes, are reported in Tab. 2 and are compared with

the reference values of [25] obtained with a spectral method.

As a recall of the fluid and thermal fields, iso-lines of dimensionless temperature T, pressure variation p and stream function Ψ are presented in Fig. 15. This natural convection configu-

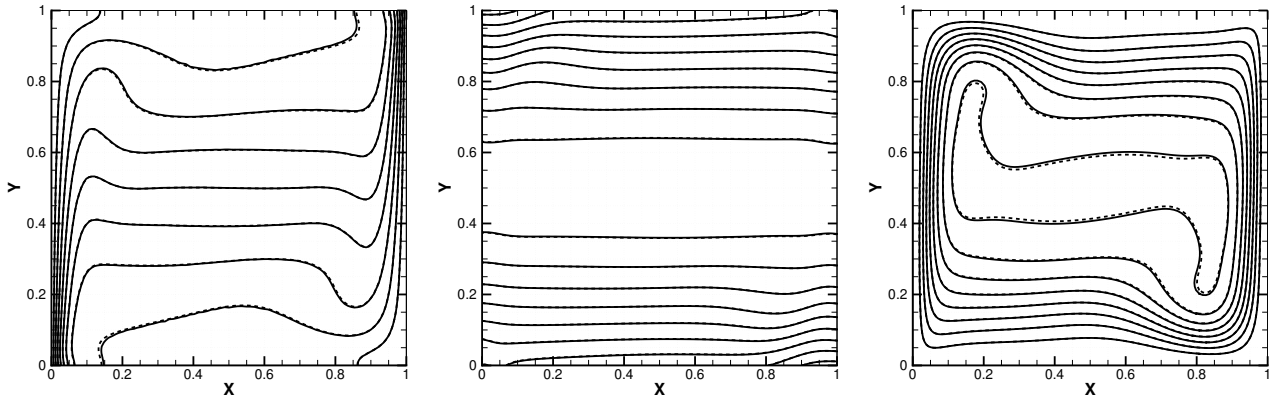

(a) T (b) p (c) Ψ

Figure 15: Iso-lines of the temperature T, $\delta T = 0.1$, pressure variation p, $\delta p = 10^5$, and stream function Ψ, $\delta\Psi = 2 \times 10^{-3}$, fields obtained with the MEL scheme (plain lines) and centered (dashed lines) schemes. The 128^2 mesh is refined near walls with a Gauss-Lobatto distribution of the cell centers.

ration does not involve high values of Péclet cell numbers, so the centered scheme is suitable and recommended for this case. However, the MEL scheme, used with four particles per direction and per cell, $P = 4$, gives very similar results to the centered scheme on a 128^2 mesh. The present benchmark simulation illustrates again the ability and adaptability of the MEL approach to represent the correct physical behavior even with for low values of the Péclet number. This problem also emphasizes the ability of the MEL to provide a discrete approximation of the advection term on irregular grids. Extension to unstructured meshes is possible.

As a quantitative comparison, values and relative difference with reference [25] are presented in Tab. 2. Except for the positions of the maximum stream function and the maximum surface Nusselt, all relative differences are lower than 1%. For the later, the error is linked to the accuracy of the reference solution; the variation of the last digit produces the 2.5% relative difference. This is a very nice result of the Mixed Eulerian-Lagrangian scheme: it can be used preferably for high Péclet problems, but also for problem involving low advection compared to diffusion. This can be the case for turbulent problems containing dead flow zones driven by diffusion, as can be encountered in air quality models with pollutant transport.

4 Concluding remarks

In the present work, the efficiency of a Mixed Eulerian-Lagrangian (MEL) method has been evaluated and demonstrated in the framework of the resolution of the advection-diffusion equation. It is even more effective when the ratio between advection and diffusion is important. The extra cost of the particle tracking method used by the MEL approach is counterbalanced by the fact that the Lagrangian advection process does not introduce numerical diffusion and

method	MEL, $P=4$						centered		spectral
N^2	32^2		64^2		128^2		128^2		Ref. [25]
$\Psi(1/2,1/2)\times 10^3$	16.526	(0.8)	16.436	(0.3)	16.444	(0.3)	16.782	(2.4)	16.386
$\Psi_{\max}\times 10^3$	16.755	(-0.3)	16.798	(0.1)	16.839	(0.2)	16.788	(-0.1)	16.811
x	0.146	(-2.7)	0.146	(-2.7)	0.154	(2.7)	0.146	(-2.7)	0.150
y	0.548	(0.2)	0.551	(0.7)	0.548	(0.2)	0.549	(0.4)	0.547
$u_{\max}(1/2,y)\times 10^2$	6.711	(3.5)	6.542	(0.9)	6.511	(0.4)	6.483	(0.0)	6.483
y	0.862	(1.4)	0.852	(0.2)	0.850	(0.0)	0.850	(0.0)	0.850
$v_{\max}(x,1/2)\times 10$	2.243	(1.7)	2.214	(0.3)	2.210	(0.2)	2.207	(0.1)	2.206
x	0.037	(-2.6)	0.037	(-2.6)	0.038	(0.0)	0.038	(0.0)	0.038
$\bar{Nu}$	8.783	(-0.5)	8.805	(-0.2)	8.814	(-0.1)	8.825	(0.0)	8.825
$Nu_{\max}$	17.610	(0.4)	17.940	(2.3)	17.544	(0.1)	17.552	(0.1)	17.536
y	0.059	(51.3)	0.038	(-2.5)	0.038	(-2.5)	0.039	(0.0)	0.039
$Nu_{\min}$	0.9873	(0.8)	0.9863	(-1.3)	0.9904	(1.1)	0.9811	(0.2)	0.9795
y	0.997	(-0.3)	0.999	(-0.1)	0.999	(-0.1)	0.999	(-0.1)	1.000

Table 2: Characteristic values for $Pr = 0.71$ and $Ra = 10^6$ with MEL and centered schemes. The bracketed values stand for the relative difference (in %) with the spectral reference [25] which is recalled in the last column. Note that the reference length and velocity are, respectively, H and $(\kappa/H)\sqrt{Ra}$ with κ the thermal diffusion coefficient.

allows the use of coarser meshes, contrary to more classical approaches. The particle tracking also involves interpolation method for the fluid velocity at the particle positions and a temporal integrator. Although it was not as detailed as the grid or the particle density number influences, these points have been studied on the presented cases. It comes out that the use of a high level interpolation method PERM [29] does not have a significant influence on the result compared to a classical linear interpolation method. This later even reduces the computational cost. Similarly, using high order Runge-Kutta schemes for particle motion does not influence the results.

The major drawback of the Lagrangian approach is the spurious oscillations introduced by the reseeding procedures. Nevertheless, they decrease with the numbers of markers which makes the scheme Essentially Non Oscillating (ENO). Several improvements could be investigated (local seeding ratio instead of global criterion for example, or the use of kernel function and averaging technique from Smooth Particle Hydrodynamics) which would also allow to reduce the number of particles involved and therefore the computational cost and memory requirements.

Finally, the method is quite straightforward to implement; it requires the ability to track Lagrangian particles (fluid flow tracers) and is not restricted to staggered regular grids. Once the particles belonging to a cell of an unstructured mesh (of polyhedral to be general) are identified, the rest of the method remains unchanged and can be easily set up.

Acknowledgements

The authors are grateful for access to the computational facilities of the French CINES (National Computing Center For Higher Education) and CCRT (National Computing Center of CEA)

under project number A0052B06115.

A Analytical solutions

The analytical solutions used in Sect. 3 for the one- and two-dimensional cases are given here. They are both obtained with the separation of variables method (see for example [32]).

A.1 Orthogonal symmetric case

A symmetrical scalar field c is initialized near the symmetry axis, for $x \in [0; \ell_0]$, and diffuses in the domain $[0, L]$, $L > \ell_0$. For $x = L$, it takes the value c_∞. In Cartesian coordinates, the following one-dimensional problem is then considered for the reduced variable $\Phi = c - c_\infty$:

$$\begin{cases} \dfrac{\partial \Phi(x,t)}{\partial t} = \Gamma \dfrac{\partial^2 \Phi(x,t)}{\partial x^2} \\ \left.\dfrac{\partial \Phi(x,t)}{\partial x}\right|_{x=0} = 0 \\ \Phi(x = L, t) = 0 \\ \Phi(x, t = 0) = \Phi^0(x) \end{cases} \tag{24}$$

where Φ^0 is the initial spatial condition and will be specified later. The function Φ is searched as $\Phi(r,t) = g(x) \times f(t)$. Introduced into the 1D unsteady diffusion equation, it shows a set of two ODEs for f and g functions given by

$$\frac{1}{\Gamma}\frac{f'(t)}{f(t)} = \frac{g''(x)}{g(x)} = \text{constant} = -\lambda^2 \tag{25}$$

The solutions are, respectively,

$$\begin{cases} g(x) = \mathcal{C}_1 \sin(\lambda x) + \mathcal{C}_2 \cos(\lambda x) \\ f(t) = \mathcal{C}_3 \exp(-\lambda^2 \Gamma t) \end{cases} \tag{26}$$

or

$$\Phi(x,t) = [\mathcal{C}_1' \sin(\lambda x) + \mathcal{C}_2' \cos(\lambda x)] \exp(-\lambda^2 \Gamma t) \tag{27}$$

with $\mathcal{C}_1' = \mathcal{C}_1\mathcal{C}_3$ and $\mathcal{C}_2' = \mathcal{C}_1\mathcal{C}_2$. From the symmetry boundary condition, $\mathcal{C}_1' = 0$. The imposed value at $x = L$ leads the $\cos(\lambda L) = 0$. To each root $\lambda_n L$ is associated with a particular solution $\Phi_n(x,t)$ and the general solution is the linear superposition of all solutions:

$$\Phi(x,t) = \sum_{n=0}^{\infty} A_n \cos\left(\frac{(2n+1)\pi}{2L}x\right) \exp\left(-\frac{(2n+1)^2\pi^2}{4L^2}\Gamma t\right) \tag{28}$$

Introducing the initial condition $\Phi^0(x)$, the A_n coefficients are given by

$$A_n = \frac{2}{L}\int_0^L \Phi^0(x) \cos\left(\frac{(2n+1)\pi}{2L}x\right) dx \tag{29}$$

In the case of a "conic" spot, where

$$\Phi^0(x) = \begin{cases} \dfrac{\ell_0 - x}{\ell_0} & \text{if } x \leq \ell_0 \\ 0 & \text{otherwise} \end{cases} \tag{30}$$

the coefficients A_n are,

$$A_n = -\frac{8L}{(2n+1)^2\pi^2\ell_0} \cos\left(\frac{(2n+1)\pi\ell_0}{2L} - 1\right) \tag{31}$$

Note that this solution is suitable to describe the diffusion process of a local concentration profile while the signal variation is far enough from the domain limit $x = L$ where the reduced concentration is set to $\Phi = 0$. Choosing $L \gg \ell_0$ also ensures $\frac{\partial\Phi}{\partial x}\big|_{x=L} = 0$; the concentration profile is flat far away from the symmetry axis.

A.2 Axisymmetric case

An axisymmetric scalar field c is initialized near the symmetry axis, for $r \in [0; r_0]$, and diffuses in the domain $[0, R]$, $R > r_0$. For $r = R$, it takes the value c_∞. In polar coordinates, the following one-dimensional problem is then considered for the reduced variable $\Phi = c - c_\infty$:

$$\begin{cases} \dfrac{\partial\Phi(r,t)}{\partial t} = \Gamma\dfrac{1}{r}\dfrac{\partial}{\partial r}\left(r\dfrac{\partial\Phi(r,t)}{\partial r}\right) \\ \left.\dfrac{\partial\Phi(r,t)}{\partial r}\right|_{r=0} = 0 \\ \Phi(r = R, t) = 0 \\ \Phi(r, t = 0) = \Phi^0(r) \end{cases} \tag{32}$$

where Φ^0 is the initial spatial condition and will be specified later. With the classical separation of variables method (see for example [32] or [28] for a very similar case), the function Φ is searched as $\Phi(r,t) = g(r) \times f(t)$. Introduced into the 1D unsteady diffusion equation, it shows a set of two ODEs for f and g functions given by

$$\frac{1}{\Gamma}\frac{f'(t)}{f(t)} = \left[\frac{g''(r)}{g(r)} + \frac{1}{r}\frac{g'(r)}{g(r)}\right] = \text{constant} = -\lambda^2 \tag{33}$$

The solutions are, respectively,

$$\begin{cases} g(r) = \mathcal{C}_1 J_0(\lambda r) + \mathcal{C}_2 Y_0(\lambda r) \\ f(t) = \mathcal{C}_3 \exp(-\lambda^2\Gamma t) \end{cases} \tag{34}$$

where J_ν and Y_ν are ν-order Bessel functions of first and second kinds respectively, and coefficients $\mathcal{C}_1$, $\mathcal{C}_2$ and $\mathcal{C}_3$ are determined with boundary and initial conditions. With $\mathcal{C}_1' = \mathcal{C}_1\mathcal{C}_3$ and $\mathcal{C}_2' = \mathcal{C}_2\mathcal{C}_3$, the solution of the unsteady diffusion equation writes

$$\Phi(r,t) = [\mathcal{C}_1' J_0(\lambda r) + \mathcal{C}_2' Y_0(\lambda r)] \exp(-\lambda^2\Gamma t) \tag{35}$$

From the symmetry condition in $r = 0$, it comes directly $\mathcal{C}_2' = 0$. The Dirichlet condition at the domain boundary $r = R$ leads to $J_0(\lambda R) = 0$. $\lambda_n R$ is then one of the roots of the equation

$J_0(x) = 0$. To each root is associated a particular solution $\Phi_n(r,t)$ and the general solution of system (32) is then a linear superposition of all solutions:

$$\Phi(r,t) = \sum_{n=1}^{\infty} A_n J_0(\lambda_n r) \exp(-\lambda_n^2 \Gamma t) \tag{36}$$

The last coefficients A_n are obtained with the initial condition. Using the orthogonality of Bessel functions, the previous equation is rewritten, after multiplying it by $rJ_0(\lambda_m r)$ and integration, as

$$\int_{r=0}^{R} \Phi^0(r) r J_0(\lambda_m r)\, dr = \int_{r=0}^{R} \sum_{n=1}^{\infty} A_n r J_0(\lambda_n r) J_0(\lambda_m r)\, dr \tag{37}$$

that leads, when $n = m$, to

$$A_n = \frac{2\displaystyle\int_{r=0}^{R} \Phi^0(r) r J_0(\lambda_n r)\, dr}{R^2 J_1^2(\lambda_n R)} \tag{38}$$

The A_n expression can be clarified when $\Phi^0(r)$ is specified.

- In the case of a homogeneous spot, given by

$$\Phi^0(r) = \begin{cases} 1 & \text{if } r \leq r_0 \\ 0 & \text{otherwise} \end{cases} \tag{39}$$

  The integral part in the expression of A_n becomes after the substitution $x = \lambda_n r$

$$\int_{r=0}^{r_0} r J_0(\lambda_n r)\, dr = \frac{1}{\lambda_n^2} \int_{x=0}^{x_0} x J_0(x)\, dx = \frac{1}{\lambda_n^2} \left[x J_1(x)\right]_0^{x_0} \tag{40}$$

  and finally, reintroducing the r variable gives

$$A_n = \frac{2 r_0 J_1(\lambda_n r_0)}{\lambda_n R^2 J_1^2(\lambda_n R)} \tag{41}$$

- In the case of a "conic" spot, where

$$\Phi^0(r) = \begin{cases} \dfrac{r_0 - r}{r_0} & \text{if } r \leq r_0 \\ 0 & \text{otherwise} \end{cases} \tag{42}$$

  the integral part of Eq. (38) is decomposed as

$$\int_{r=0}^{r_0} \left(1 - \frac{r}{r_0}\right) r J_0(\lambda_n r)\, dr = \int_{r=0}^{r_0} r J_0(\lambda_n r)\, dr - \int_{r=0}^{r_0} \frac{r^2}{r_0} J_0(\lambda_n r)\, dr \tag{43}$$

  where the first term of r.h.s leads to the A_n coefficient obtained in Eq. (41). The substitution $x = \lambda_n r$ is used again to express the second term:

$$\begin{aligned} \int_{r=0}^{r_0} \frac{r^2}{r_0} J_0(\lambda_n r)\, dr &= \frac{1}{r_0 \lambda_n^3} \int_{x=0}^{x_0} x^2 J_0(x)\, dx \\ &= \frac{1}{r_0 \lambda_n^3} \left[x^2 J_1(x) - \frac{\pi x}{2} \left[H_0(x) J_1(x) - H_1(x) J_0(x)\right]\right]_0^{x_0} \end{aligned} \tag{44}$$

where H_ν is the ν-order Struve function. The expression of the integral $\int x^2 J_0(x)\,dx$ can be found in [34]. Finally,

$$A_n = \frac{2r_0 J_1(\lambda_n r_0)}{\lambda_n R^2 J_1^2(\lambda_n R)} - \frac{2}{r_0 R^2 J_1^2(\lambda_n R)\lambda_n^3}\left((\lambda_n r_0)^2 J_1(\lambda_n r_0) - \frac{\pi\lambda_n r_0}{2}\left[H_0(\lambda_n r_0)J_1(\lambda_n r_0) - H_1(\lambda_n r_0)J_0(\lambda_n r_0)\right]\right) \tag{45}$$

As for the orthogonal case A.1, these solutions are suitable to describe the diffusion process of a local concentration profile while the signal variation is far enough from the domain limit $r = R$.

References

[1] Amestoy, P. R., Duff, I. S., Koster, J., and L'Excellent, J.-Y. "A Fully Asynchronous Multifrontal Solver Using Distributed Dynamic Scheduling". In: *SIAM Journal on Matrix Analysis and Applications* 23.1 (2001), pp. 15–41.

[2] Campos, L., Gardin, P, Vincent, S, and Caltagirone, J. "Physical modeling of turbulent multiphase flow in a continuous casting steel mold". In: *Computational Methods in Multiphase Flow VIII* 89 (2015), pp. 439–450.

[3] Chertock, A., Kurganov, A., and Petrova, G. "Fast explicit operator splitting method for convection–diffusion equations". In: *International Journal for Numerical Methods in Fluids* 59.3 (2006), pp. 309–332.

[4] Cottet, G.-H. "Multi-physics and particle methods". In: *Computational Fluid and Solid Mechanics* (2003), pp. 1296–1298.

[5] Couderc, F. "Development of a numerical code for the simulation of non-miscible fluid flow. Application to the air-assisted disintegration of a liquid jet." Theses. Ecole nationale superieure de l'aeronautique et de l'espace, Feb. 2007.

[6] De Vahl Davis, G. and Jones, I. P. "Natural convection in a square cavity: A comparison exercise". In: *International Journal for Numerical Methods in Fluids* 3.3 (1983), pp. 227–248.

[7] Delage, S., Vincent, S., Caltagirone, J.-P., and Heliot, J.-P. "A hybrid linking approach for solving the conservation equations with an adaptive mesh refinement method". In: *Journal of Computational and Applied Mathematics* 191.2 (2006), pp. 280–296.

[8] Deng, L., Zhang, Y., Wen, Y., Shan, B., and Zhou, H. "A fractional-step thermal lattice Boltzmann model for high Peclet number flow". In: *Computers & Mathematics with Applications* 70.5 (2015), pp. 1152 –1161.

[9] Devkota, B. H. and Imberger, J. "Lagrangian modeling of advection-diffusion transport in open channel flow". In: *Water resources research* 45.12 (2009).

[10] Dugois, K., Vincent, S., Lasseux, D., Arquis, E., and Descamps, C. "A macroscopic model for the impregnation process of composite material by a concentrated suspension". In: *European Congress and Exhibition on Advanced Materials and Processes, Warsaw, Poland, September 20–24* (2015).

[11] Enright, D., Losasso, F., and Fedkiw, R. "A fast and accurate semi-Lagrangian particle level set method". In: *Computers & Structures* 83.6 (2005). Frontier of Multi-Phase Flow Analysis and Fluid-Structure, pp. 479 –490.

[12] Geiser, J. and Elbiomy, M. *Splitting Method of Convection-Diffusion Methods with Disentanglement methods*. Humboldt-Universität zu Berlin, Mathematisch-Naturwissenschaftliche Fakultät II, Institut für Mathematik, 2011.

[13] Grassia, P. and Ubal, S. "Streamline-averaged mass transfer in a circulating drop". In: *Chemical Engineering Science* 190 (2018), pp. 190 –219.

[14] Guichard, R. and Belut, E. "Simulation of airborne nanoparticles transport, deposition and aggregation: Experimental validation of a CFD-QMOM approach". In: *Journal of Aerosol Science* 104 (2017), pp. 16–31.

[15] Gustafsson, I. *On first and second order symmetric factorisation methods for the solution of elliptic difference equations*. Chalmers University of Technology, 1978.

[16] Halim Atallah, G., Trouette, B., Belut, E., Vincent, S., and Lechène, S. "LES simulation of pollutant transport in ventilation-based mitigation devices". In: *Turbulence and Interactions 2018 (TI2018), 25-29 June, Martinique, France* (2018).

[17] Harlow, F. and Welch, J. "Numerical calculation of time-dependent viscous incompressible flow of fluid with free surface". In: *Physics of Fluids* 8 (1965), pp. 2182–2189.

[18] Hermes, V., Klioutchnikov, I., and Olivier, H. "Linear stability of WENO schemes coupled with explicit Runge–Kutta schemes". In: *International Journal for Numerical Methods in Fluids* 69.6 (2012), pp. 1065–1095.

[19] Hirsch, C. *Numerical Computation of Internal and External Flows: The Fundamentals of Computational Fluid Dynamics*. Elsevier, 2007.

[20] Hoover, W. *Smooth Particle Applied Mechanics*. World Scientific, 2006.

[21] Jiang, G.-S. and Shu, C.-W. "Efficient Implementation of Weighted ENO Schemes". In: *Journal of Computational Physics* 126.1 (1996), pp. 202 –228.

[22] Khadra, K., Angot, P., Parneix, S., and Caltagirone, J.-P. "Fictitious domain approach for numerical modelling of Navier–Stokes equations". In: *International journal for numerical methods in fluids* 34.8 (2000), pp. 651–684.

[23] Khalili, A., Basu, A., Pietrzyk, U., and Jørgensen, B. B. "Advective transport through permeable sediments: a new numerical and experimental approach". In: *Acta mechanica* 132.1-4 (1999), pp. 221–227.

[24] Koumoutsakos, P. "Multiscale flow simulations using particles". In: *Annu. Rev. Fluid Mech.* 37 (2005), pp. 457–487.

[25] Le Quéré, P. "Accurate solutions to the square thermally driven cavity at high Rayleigh number". In: *Computers & Fluids* 20.1 (1991), pp. 29 –41.

[26] LeVeque, R. J. "High-resolution conservative algorithms for advection in incompressible flow". In: *SIAM Journal on Numerical Analysis* 33.2 (1996), pp. 627–665.

[27] Liu, C.-H., Barth, M. C., and Leung, D. Y. "Large-eddy simulation of flow and pollutant transport in street canyons of different building-height-to-street-width ratios". In: *Journal of Applied Meteorology* 43.10 (2004), pp. 1410–1424.

[28] Mackowski, D. W. "Conduction Heat Transfer: Notes for MECH 7210". In: *Mechanical Engineering Department, Auburn University* (2011).

[29] McDermott, R. and Pope, S. B. "The parabolic edge reconstruction method (PERM) for Lagrangian particle advection". In: *Journal of Computational Physics* 227.11 (2008), pp. 5447–5491.

[30] Monaghan, J. J. "An introduction to SPH". In: *Comput. Phys. Comm.* 48 (1988), pp. 89–96.

[31] Nguyen, K. and Dabdub, D. "Two-level time-marching scheme using splines for solving the advection equation". In: *Atmospheric Environment* 35.9 (2001), pp. 1627–1637.

[32] Poulikakos, D. *Conduction Heat Transfer*. Ed. by Prentice-Hall. 1993.

[33] Rapaport, D. C. *The art of molecular dynamics simulation*. Cambridge university press, 2004.

[34] Rosenheinrich, W. "Tables of some indefinite integrals of Bessel functions". In: *University of Applied Sciences, Germany* (2012).

[35] Sarra, S. A. "The method of characteristics with applications to conservation laws". In: *Journal of Online mathematics and its Applications* 3 (2003), pp. 1–16.

[36] Shadloo, M., Oger, G., and Touzé], D. L. "Smoothed particle hydrodynamics method for fluid flows, towards industrial applications: Motivations, current state, and challenges". In: *Computers & Fluids* 136 (2016), pp. 11 –34.

[37] Shu, C.-W. and Osher, S. "Efficient implementation of essentially non-oscillatory shock-capturing schemes". In: *Journal of Computational Physics* 77.2 (1988), pp. 439 –471.

[38] Sorek, S. "Eulerian-Lagrangian method for solving transport in aquifers". In: *Advances in water resources* 11.2 (1988), pp. 67–73.

[39] Spiegelman, M. and Katz, R. F. "A semi-Lagrangian Crank-Nicolson algorithm for the numerical solution of advection-diffusion problems". In: *Geochemistry, Geophysics, Geosystems* 7.4 (2006).

[40] Sun, Z. and Xiao, F. "A semi-Lagrangian multi-moment finite volume method with fourth-order WENO projection". In: *International Journal for Numerical Methods in Fluids* 83.4 (2017), pp. 351–375.

[41] Vincent, S. and Caltagirone, J.-P. “Efficient solving method for unsteady incompressible interfacial flow problems”. In: *International Journal for Numerical Methods in Fluids* 30.6 (1999), pp. 795–811.

[42] Vincent, S., Balmigère, G., Caltagirone, J.-P., and Meillot, E. “Eulerian–Lagrangian multiscale methods for solving scalar equations – Application to incompressible two-phase flows”. In: *Journal of Computational Physics* 229.1 (2010), pp. 73 –106.

[43] Wacławczyk, M., Pozorski, J., and Minier, J.-P. “New molecular transport model for FDF/LES of turbulence with passive scalar”. In: *Flow, turbulence and combustion* 81.1-2 (2008), p. 235.

[44] Zahran, Y. H. “An efficient TVD-WENO method for conservation laws”. In: *Numerical Methods for Partial Differential Equations: An International Journal* 25.6 (2009), pp. 1443–1467.

[45] Zimmermann, S., Koumoutsakos, P., and Kinzelbach, W. “Simulation of pollutant transport using a particle method”. In: *Journal of Computational Physics* 173.1 (2001), pp. 322–347.

[46] van der Vorst, H. A. “Bi-CGSTAB: a fast and smoothly converging variant of Bi-CG for the solution of nonsymmetric linear systems”. In: *SIAM Journal of Scientific Statistical Computing* 13 (1992), pp. 631–644.